Soft Matter

PAPER

View Article Online
View Journal | View Issue

Cite this: *Soft Matter*, 2020, **16**, 9273

Shaving and breaking bacterial chains with a viscous flow†

Faustine Gomand, *[ab] William H. Mitchell, [c] Jennifer Burgain,[a] Jérémy Petit,[a] Frédéric Borges,[a] Saverio E. Spagnolie*[b] and Claire Gaiani [a]

Received 19th February 2020,
Accepted 3rd August 2020

DOI: 10.1039/d0sm00292e

rsc.li/soft-matter-journal

Some food and ferment manufacturing steps such as spray-drying result in the application of viscous stresses to bacteria. This study explores how a viscous flow impacts both bacterial adhesion functionality and bacterial cell organization using a combined experimental and modeling approach. As a model organism we study *Lactobacillus rhamnosus* GG (LGG) "wild type" (WT), known to feature strong adhesive affinities towards beta-lactoglobulin thanks to pili produced by the bacteria on cell surfaces, along with three cell-surface mutant strains. Applying repeated flows with high shear-rates reduces bacterial adhesive abilities up to 20% for LGG WT. Bacterial chains are also broken by this process, into 2-cell chains at low industrial shear rates, and into single cells at very high shear rates. To rationalize the experimental observations we study numerically and analytically the Stokes equations describing viscous fluid flow around a chain of elastically connected spheroidal cell bodies. In this model setting we examine qualitatively the relationship between surface traction (force per unit area), a proxy for pili removal rate, and bacterial chain length (number of cells). Longer chains result in higher maximal surface tractions, particularly at the chain extremities, while inner cells enjoy a small protection from surface tractions due to hydrodynamic interactions with their neighbors. Chain rupture therefore may act as a mechanism to preserve surface adhesive functionality in bacteria.

1 Introduction

Lactic acid bacteria (LAB) are commonly used as starter cultures in food manufacturing, especially for dairy products.[1–4] Recently, they have also been increasingly used for functional food design, due to their probiotic potential *i.e.* their ability to provide health benefits to their host.[4] Food manufacturing, storage, and digestion conditions, as well as food matrix structure and composition have been shown to markedly affect LAB probiotic abilities.[5–7] In order to benefit human health, LAB cells need to remain not only viable but also functional, *i.e.* able to interact with their host through adhesive interactions and to multiply.[7]

Factors likely to influence LAB adhesion are numerous. For example, environmental stresses can lead to the loss or inactivation of bacterial surface biomolecules modulating bacterial-host interactions and adhesion.[8] Bacterial stress can occur in a wide variety of situations including common food and ferment manufacturing steps, such as acid stress during fermentation,[9] heat stress upon drying,[10] and shear stress occurring during spray-drying and extrusion processes[10–18] as well as during the biological process of digestion.[19,20] In this article, we chose to focus on the effect of shear stress on the functionality of the model probiotic strain *Lactobacillus rhamnosus* GG (LGG).

LGG features well-known adhesive capacities mediated by pili, which are filamentous, proteinaceous surface appendages found both in Gram-negative and Gram-positive bacteria.[21–26] LGG pili are helical-shaped (spring-like) and measure about 1.0 ± 0.3 μm for a diameter of 5 ± 1 nm, with a persistence length of 0.4 nm.[27] They are mostly concentrated at the poles of a given bacterium and each bacterium features between 10 and 50 pili.[27] Previous studies pointed out that shear stress may cause partial or even total removal of pili.[28,29] Still, little investigation has been done on this topic and most of the existing studies concerned Gram-negative bacteria responsible for infections.[30–38]

Some cases of shear-enhanced cell metabolism were found amongst lactic acid bacteria (LAB) for *Lactobacillus delbrueckii* subsp. *bulgaricus* at intermediate shear rates.[11] High shear forces

[a] *LIBio - Université de Lorraine, 2 avenue de la Forêt de Haye, 54500 Vandoeuvre-lès-Nancy, France. E-mail: faustine.gomand@gmail.fr, claire.gaiani@univ-lorraine.fr*
[b] *Department of Mathematics, University of Wisconsin-Madison, 480 Lincoln Dr., Madison, WI 53706, USA. E-mail: spagnolie@math.wisc.edu*
[c] *Department of Mathematics, Statistics, and Computer Science, Macalester College, 1600 Grand Ave, St. Paul, MN 55105, USA. E-mail: wmitchel@macalester.edu*

† Electronic supplementary information (ESI) available: Complete data set for microscopic observations on bacterial chain distribution. See DOI: 10.1039/d0sm00292e

could weaken bacterial cells[11,39] and may even cause inhibition of microbial growth and productivity (turbohypobiosis).[39] Only two studies describe the impact of shearing on the adhesive abilities of LAB.[29,40] *Lactobacillus kefir* 8321 and *Lactobacillus plantarum* 83 114 were found to be still able to adhere to intestinal cells after spray-drying for atomizing air pressures of 3 bars whereas the strain *Lactobacillus kefir* 8348 showed a significant loss of adhesion capacity.[40] In the case of LGG, high shear rates were shown to completely shear off pili and significantly affect adhesion ability to Caco-2 cells.[29] These two studies represent first steps in the direction of a better understanding on how food and ferment manufacturing steps may affect bacterial functionality. However, they do not distinguish between the different stresses (shear, heat, and osmotic) resented during spray-drying, which may altogether impact pili expression and functionality, both being crucial to bacterial probiotic action.

In addition to impact bacterial functionality, shear stress may also cause bacterial chain fragmentation.[10,15,29] Very little is known about why some bacteria may organize preferentially in chains *versus* filaments or isolated cells, and whether bacterial chain breakage may be beneficial or detrimental to their survival and functionality in stressful environments. Possible rationales were proposed to relate bacterial shape and organization to the evolutionary process and their survival value, such as enhanced nutrient access and escaping from predators.[41,42]

Chaining may help with survival in high shear or grazing environments, by enhancing biofilm formation, increasing the number of contacts intertwining with surface elements to resist detachment,[13] and provide selective advantage against predation in grazing environments.[43–47] When competing for similar resources, some strains such as *Lactococcus lactis* may induce chain fragmentation amongst their competitors by producing lysins.[41,48] Similarly, bacterial filamentation may also provide competitive advantages for colonization of biopassive surfaces.[49] Shear stress may favor filamentation as increasing calcium ion transfer that plays an important role in osmoregulation phenomena leading to cell wall stretching and bacterial cell elongation.[12,16]

If chaining and cell elongation may appear as competitive advantages in terms of survival in stressful environments, they have rarely been looked at in relation to bacterial functionality. Only one study suggests that bacterial organization and bacterial functionality may be correlated in the case of *Lactobacillus acidophilus*, as the gene identified to be responsible for cell-division and cell elongation, *cdpA*, was found to control bacterial adhesion abilities as well.[50] No study that we could find proposed a rationale that may relate bacterial functionality and organizational adaptation under stressful conditions.

This article aims to fill this gap by providing a multi-scale insight on the impact of shear stress on bacterial viability and functionality in relation to bacterial organization, in chains, flocs, and isolated cells, using a combined experimental and theoretical approach. Experiments focus on the collective behavior of bacterial suspensions whereas simulations are useful to propose rationales at the cell level. Material and methods (both experimental and numerical) used in the study are detailed in Section 2, with a focus on the determination of the characteristic shear rates correlated to the range of air pressures used. In Section 3, we describe experiments in which shear stress is applied to bacterial suspensions, mimicking the shearing phase of a spray-drying process. Both bacterial chain fragmentation and changes in bacterial adhesive functionality were monitored. In particular, the impact of shear stress on the pili of the model strain *Lactobacillus rhamnosus* GG (LGG) and three surface mutant strains was investigated, using the method developed by Gomand *et al.* (2018).[51] One great advantage of this method consists in allowing the simultaneous determination of bacterial adhesive abilities and viability, thus providing a more global insight on the maintenance of probiotic abilities in response to stress. The use of mutant strains was necessary to investigate separately the roles of several different bacterial cell wall elements in response to shear stress. Combining these results therefore helped with a better understanding of the wild type strain response.

Numerical solution of the Stokes equations describing viscous flow, and a few theoretical predictions aimed towards rationalizing our experimental observations, are introduced in Section 4. Viscous traction (force per unit area) is predicted to result in bacterial cell "shaving," removing and/or damaging surface proteins including pili; they can also be correlated with chain breakage. The tractions experienced by the individual cells in a chain are found to vary with both chain length, due in part to chain deformability, and cell position within a chain. Finally, in Section 5 a relationship between bacterial chain fragmentation and bacterial functionality preservation in shearing environments is proposed, combining results obtained from both approaches.

2 Experimental

2.1 Experimental shearing

2.1.1 Bacterial strains and cultures. Four strains were studied: the model strain *Lactobacillus rhamnosus* GG ATCC53103 (LGG wild type, "WT") and three derivative mutant strains LGG *spaCBA* CMPG 5357, impaired in pili synthesis,[27] LGG *welE* CMPG 5351, impaired in exopolysaccharides (EPS) production,[52] and LGG *welE-spaCBA* CMPG 5355 ("D2"), double mutant[25] impaired both in pili synthesis and exopolysaccharides production. The adhesion properties of these strains have been previously described.[24,25,27,28]

All strains were pre-cultivated at 37 °C overnight in 10 mL of MRS medium (de Man, Rogosa and Sharpe) inoculated with 100 μL of frozen cultures previously stored at −80 °C. The next day, 100 μL of the pre-cultures were used to inoculate 10 mL of MRS medium and the suspensions were left for incubation at 37 °C until they reached an optical density of 0.8 at 595 nm. Bacterial suspensions were then centrifuged at 3618 g for 10 min at ambient temperature. The resulting cell pellets were resuspended in phosphate buffered saline

(PBS, P4417, Sigma-Aldrich Co. LLC, St Louis, MO, USA) adjusted at pH 6.8 and the resulting bacterial suspensions were subsequently used for shearing experiments. Triplicates on independent cultures were performed as well as six replicates of shearing experiments by strain for a given culture.

2.1.2 Preparation of the protein solutions and microplate coating. β-Lactoglobulin (Sigma-Aldrich Co. LLC, St Louis, MO, USA) and BSA (Sigma-Aldrich Co. LLC, St Louis, MO, USA) solutions (1% w/w) were prepared as described by Gomand *et al.*[51] Briefly, solutions were left homogenizing for a minimum of 2 h, and then 200 µL per well were introduced in high-binding 96-well microplates, one half of each microplate containing β-lactoglobulin-filled wells, and the other half containing BSA-filled wells. Microplates were stored overnight at 9 °C to allow biomolecules immobilization. Wells were washed twice the next day with 300 µL of PBS supplemented with the blocking reagent Tween 20 (PBST, 5% Tween 20 v/v, pH adjusted at 6.8), and subsequently used for adhesion assays.

2.1.3 Experimental system. Bacterial adhesion to β-lactoglobulin and bacterial chain size distribution were experimentally evaluated on model strains before and after shearing in order to estimate the impact of shear stress on bacterial functionality and organization. In this study, bacterial adhesion was considered to constitute an indicator of bacterial surface integrity. Bacterial adhesion to bovine serum albumin (BSA) was also recorded as a negative control, owing to the low adhesive affinity of LGG for BSA.[24,51,53] A general overview of the experimental setup is displayed in Fig. 1.

2.1.4 Shearing experiments and calculation of spray-drying characteristic shear rates. Bacterial suspensions were sheared using a bi-fluid nozzle composed of a Fluid Cap 60100 and an Air Cap 120 (Spraying Systems Co., Wheaton, IL, USA; inner and outer diameters of the liquid channel: D_{i_L} = 1.524 mm and D_{o_L} = 2.540 mm; air channel inner diameter: D_A = 3.048 mm). The bacterial suspension was pumped into the nozzle through a 48-mm tube using a peristaltic pump (VWR International Europe bvba, Leuven, Belgium) such as presented in Fig. 1. Liquid flow rate was fixed at $\dot{q}_B = 20.3 \pm 0.32$ mL s^{-1}. Shear rate was monitored by modifying the air pressure (0.2, 0.4, 0.6, 1, and 4 bars).

A review on two-fluid atomization written by Hede *et al.* (2008)[54] and a study performed by Ghandi *et al.* (2012)[14] were used to calculate the shear rates corresponding to the investigated range of air pressures. The review by Hede *et al.* helped taking into account the role of formulation, nozzle geometry, and feed and gas flow rates for two-fluid nozzles introducing basic nozzle theory and thermodynamics, and can be referred to for more detailed information on these matters.[54] Ghandi *et al.* (2012) give directions we used to determine characteristic shear rates for an external mixing two-fluid nozzle such as represented in Fig. 2 from the velocities of air and bacterial suspension v_A, v_B, the mass flow rates of air and bacterial suspension $\dot{m}_A$, $\dot{m}_B$, and nozzle characteristics (diameters D_{i_L}, D_{o_L}, D_A).

Characteristic shear rates were calculated based on the two following equations:[14]

$$\dot{\gamma} = \frac{2(v_{av} - v_B)}{D_{i_L}} \quad (1)$$

$$v_{av} = \frac{v_A \dot{m}_A + v_B \dot{m}_B}{\dot{m}_A + \dot{m}_B} \quad (2)$$

Here v_{av} is the average velocity in the mixing zone, assuming transfer of momentum between the bacterial suspension and

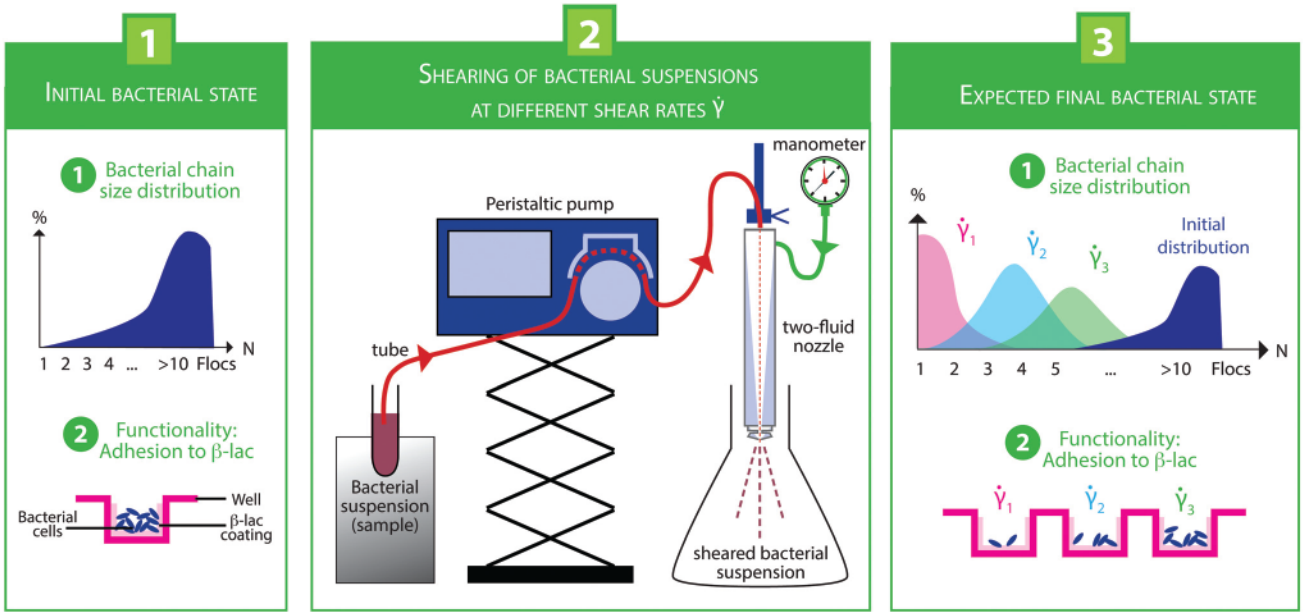

Fig. 1 Overview of the experimental setup allowing the determination of the impact of shear stress on bacterial functionality (through bacterial adhesion) and bacterial organization (through bacterial chain size distribution); "β-lac" stands for "β-lactoglobulin".

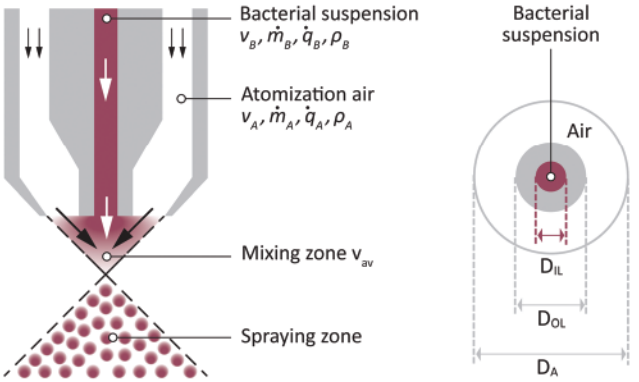

Fig. 2 Vertical (left) and horizontal (right) cross-sections of the external two-fluid nozzle used for shearing experiments, adapted from Ghandi *et al.* (2012).[14] Bacterial suspension and atomization air respectively have velocities v_B, v_A, mass flow rates $\dot{m}_B$, $\dot{m}_A$, volumetric flow rates $\dot{q}_B$, $\dot{q}_A$, and densities ρ_B, ρ_A; inner and outer diameters of the liquid channel: D_{i_L}, D_{o_L}; air channel inner diameter: D_A.

air which both leave the atomization zone at constant velocities, respectively v_B and v_A. Air and liquid velocities were calculated using the following relationships:

$$v_A = \dot{q}_A \left(\frac{\pi D_A^2}{4} - \frac{\pi D_{O_L}^2}{4} \right)^{-1} \quad (3)$$

$$v_B = \frac{4\dot{q}_B}{\pi D_{i_L}^2} \quad (4)$$

The liquid and air volumetric flow ratesn $\dot{q}_B$, $\dot{q}_A$ were determined experimentally; $\dot{q}_B$ was found to be independent of applied air pressure, and $\dot{q}_A$ was measured at ambient temperature (20 °C) using a gas meter (Gallus G4, Itron) for air pressures of 0.2, 0.4, 0.6, and 1 bar. This experimental set of flow rates was combined with the nominal flow rate at 4 bars given by the supplier in the technical sheet and a polynomial model was fitted allowing linking the air flow rate to the air pressure (with $\dot{q}_A$ in L min^{-1}, P in bars, and dimensional numerical values):

$$\dot{q}_A = -1.67P^2 + 26.78P + 30.58,\ R^2 = 0.999 \quad (5)$$

The mass flow rates have been calculated using the relation $\dot{m} = \rho\dot{q}$ where ρ is the fluid density (in kg m^{-3}) and $\dot{q}$ the volumetric flow rate (m^3 s^{-1}). The bacterial suspension density ρ_B has been averaged experimentally on 10 samples of 10 mL of bacterial suspension in PBS with an optical density of 0.8. The relevant parameters used to calculate characteristic shear rates have been gathered in Table 1.

For each air pressure, 5 mL of sheared bacterial suspension were sampled at about 50 cm of the nozzle exit. Five milliliters of sheared bacterial suspension were also collected when no air pressure was applied, to determine whether going through the nozzle itself could impact bacterial functionality. In this case, the shear rate was determined using the following formula:

$$\dot{\gamma} = \frac{2v_B}{D_{i_L}} \quad (6)$$

Table 1 Parameters used to determine the characteristic shear rates used in shearing experiments. The different values of $\dot{q}_A$ correspond to different air pressures (0.2, 0.4, 0.6, 1, and 4 bars). "NA" means "non applicable"

Parameter	Bacterial suspension	Air
D_{i_L} (mm)	1.524	NA
D_{o_L} (mm)	2.540	NA
D_A (mm)	NA	3.048
ρ (kg m^{-3})	1025.8	1.204
$\dot{q}$ (L min^{-1})	$20.3 \times 10^{-3} \pm 0.32$	34.8 ± 0.4
		41.8 ± 0.4
		47.2 ± 0.7
		54.8 ± 1.2
		111 (fitted nominal value)

Table 2 Characteristic shear rates and air pressures applied in shearing experiments

Air pressure (bar)	Characteristic shear rate (10^5 s^{-1})
0	0.00244
0.2	3.0
0.4	3.7
0.6	4.2
1.0	4.9
4.0	11

Based on these calculations, the characteristic shear rates investigated in shearing experiments have been gathered in Table 2.

A linear relationship can be established between the air pressure and shear rate:

$$\dot{\gamma} \approx (1.93 \times 10^5)P + (2.89 \times 10^5),\ R^2 = 0.996 \quad (7)$$

with $\dot{\gamma}$ in s^{-1} and P in bars.

The influence of repeated shear stress was also studied by shearing three times the same bacterial suspension.

2.1.5 Functionality assessment. Bacterial functionality was evaluated through bacterial adhesion to β-lactoglobulin using the method described by Gomand *et al.* (2018).[51] Briefly, sheared and control (without shearing) bacterial suspensions were diluted until reaching an optical density of 0.5 at 595 nm. One hundred and twenty microliters of diluted sampled were then introduced into each well of the high-binding 96-well microplates containing immobilized β-lactoglobulin and BSA and left 1 h for incubation at 37 °C. Each well was then washed 5 times using 300 μL of PBST (pH 6.8) to eliminate non-adherent strains. Two hundred microliters of MRS were finally introduced into each well and bacterial growth was monitored through measurements of optical density at 595 nm over 20 h. The quicker the apparent growth started, the higher the bacterial affinity towards β-lactoglobulin, *i.e.* the less shear-impacted the bacterial suspension. Strain growth comparison was performed using times at which the apparent bacterial growth starts (right after the lag phase), called t_{start}, and results have been expressed in terms of $1000/t_{start}$ to match high adhesion abilities with high values.[51]

2.1.6 Bacterial chain size distribution assessment. Bacterial chain distribution was evaluated through microscopic observations.

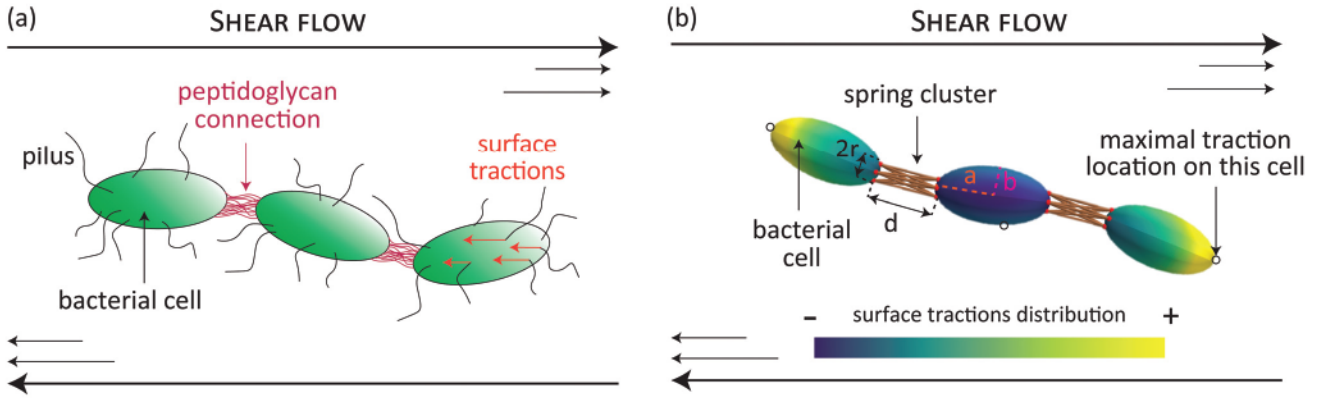

Fig. 3 Visual representation of a model 3-cell bacterial chain in a shear flow (a) and output of the numerical model with full hydrodynamic color scale for surface tractions that is reset every time step (b); a, $b = a/2$, $r = 0.3a$, and $d = a$ are respectively the half-length and half-width of each model bacterium, the radius of the spring cluster connecting them, and the spring resting length.

For each assay, 5 μL of half-diluted sheared and control bacterial suspension were sampled, dried, stained with crystal violet, and washed with distilled water. Microscopic observations were performed using an Olympus microscope (Olympus Corp., Shinjuku, Tokyo, Japan) alongside with Toupcam software (ToupTek Photonics, Zhejiang, P.R. China). Thirty pictures by sample were taken and analyzed.

2.1.7 Data treatment and statistics. Bacterial functionality results were normalized for each shearing experiment using the measured adhesion of control LGG WT (before shearing) to β-lactoglobulin. Cross-analysis were performed *via* Tukey HSD (honestly significant difference) tests (parametric for multiple comparisons) for normal data and Steel-Dwass tests (non-parametric for multiple comparisons) for data that did not fit normal distribution using Kyplot software (Kyens Lab Inc.) to highlight the main observed differences according to shearing conditions for each strain.

2.2 Mathematical model and numerical method

To better understand the dynamics and shear-stresses experienced by bacterial chains we study the Stokes equations, the zero Reynolds number‡ limit of the Navier-Stokes equations describing viscous fluid flow. In this limit the fluid pressure p and velocity $\boldsymbol{u}$ satisfy momentum balance, $-\nabla p + \mu\nabla^2\boldsymbol{u} = 0$, and mass conservation, $\nabla\cdot\boldsymbol{u} = 0$. Even with large injection rates we estimate the Reynolds number at the bacterial cell level (using $L \approx 0.5$ μm) is less than 10^{-1}.

Model chains of bacteria will be represented as linked chains of identical, rigid spheroidal bodies of length $2a$ and width $2b$ as illustrated in Fig. 3, connected to one another by clusters of 16 springs. In reality, connections between cells are mostly constituted of peptidoglycans (Fig. 3a) which are covalently closed meshwork of rigid glycan strands cross-linked by relatively flexible peptide bridges.[55] The Stokes equations are solved numerically to high accuracy using a boundary integral representation of the flow,[56] specifically the completed traction boundary integral equation as derived and implemented in ref. 57. This approach simultaneously returns the rigid body velocities of each cell and the spatially varying surface traction (force per unit area), $\boldsymbol{f}$, which we will use to evaluate the extent of the flow-induced damage to the bacterial cell surface. Specifically, with D_q the boundary of the qth body with centroid $\boldsymbol{Y}^q$, the rigid body translational velocity $\boldsymbol{U}^q$ and rotational velocity $\boldsymbol{\Omega}^q$ are found by solving a system of integral equations,

$$\begin{aligned}
&\frac{1}{8\pi}\int_{D_q} T_{ijk}(\boldsymbol{y}',\boldsymbol{y})(f_i(\boldsymbol{y}')n_k(\boldsymbol{y}) + f_i(\boldsymbol{y})n_k(\boldsymbol{y}'))\mathrm{d}S_{y'} \\
&+\sum_{p\neq q}\frac{1}{8\pi}n_k(\boldsymbol{y})\int_{D_p} T_{ijk}(\boldsymbol{y}',\boldsymbol{y})f_i(\boldsymbol{y}')\mathrm{d}S_{y'} \\
&+\sum_{p=1}^{N}\frac{1}{8\pi}\int_{D_p} C_{ij}(\boldsymbol{y}',\boldsymbol{y})f_i(\boldsymbol{y}')\mathrm{d}S_{y'} - \mu\left(U_j^q + \varepsilon_{jk\ell}\Omega_k^q(y_\ell - Y_\ell^q)\right) \\
&= -\mu(A_{jk}+A_{kj})n_k(\boldsymbol{y}) + \frac{\mu}{2}(A_{jk}-A_{kj})y_k + \frac{\mu}{2}(A_{jk}+A_{kj})Y_k^q.
\end{aligned} \tag{8}$$

Here $\boldsymbol{y}$ is a surface parameterization, $\boldsymbol{n}$ is the outward-pointing unit normal vector, and $\mathrm{d}S_{y'}$ is the infinitesimal surface area element. The undisturbed linear background fluid velocity is written as $\boldsymbol{u}^\infty(\boldsymbol{x}) = A\cdot\boldsymbol{x}$, and we set $A_{ij} = \dot\gamma\delta_{i1}\delta_{j3}$, with $\dot\gamma$ a shear rate. The kernels which appear above are $T_{ijk}(\boldsymbol{y}',\boldsymbol{y}) = -6(y_i'-y_i)(y_j'-y_j)(y_k'-y_k)|\boldsymbol{y}'-\boldsymbol{y}|^{-5}$, the free-space stresslet, and $C_{ij}(\boldsymbol{y}',\boldsymbol{y}) = \delta_{ij}/r + r_ir_j/r^3 + \varepsilon_{m\ell j}\varepsilon_{mpi}r_pr_l$ which appears as a means of flow completion (see ref. 58) with $r_i = y_i - Y_i^q$. The system is closed upon requiring each body to be force and torque free, $\int_{D_q} f_j(\boldsymbol{y})\mathrm{d}S_y = 0$, $\int_{D_q}\varepsilon_{jk\ell}r_kf_\ell(\boldsymbol{y})\mathrm{d}S_y = 0$.

We discretize the system above using a Nyström collocation scheme, employing discrete quadrature rules based on spherical coordinates with Gauss-Legendre integration in the zenith angle and the trapezoidal rule in the azimuth angle. The subtracted singularity in (8) still has a bounded jump discontinuity on D_q at $\boldsymbol{y}' = \boldsymbol{y}$, which we address by setting the integrand to zero there. The resulting linear system is dense and non-normal

‡ The Reynolds number is a dimensionless ratio of inertial to viscous dissipative forces, $\mathrm{Re} = \rho UL/\mu$, with ρ the fluid density, U and L characteristic velocity and length scales, and μ the fluid viscosity.

and we solve it using the generalized minimal residual method (GMRES). The resulting scheme is second-order accurate in the spatial grid-spacing. The body positions and orientations are evolved in time using adaptive time-stepping, which requires fewer solutions of the system above when the body motion is slowly varying, but results in small timesteps and substantial computational effort when two particles are in near contact.

The 16-spring cluster connecting neighboring cells is symmetrically distributed from four points on one body to four points on the next, each a radial distance $r = 0.3a$ away from the pole, as shown in Fig. 3. The springs are identical and Hookean with spring constant k_L and resting length d; the cluster, however, penalizes both bending and twisting modes; hydrodynamic stresses on the springs are neglected. Until the discussion of chain rupture towards the end of the paper we set $k_L/(\mu a^2\dot{\gamma}) = 350$ and $d/a = 1$ for the cases considered. In reality, the length of the connection d between two bacterial cells in a chain depends on the growth stage of each cell,[59–70] as well as on various cell division characteristics such as the physico-chemical composition of the linkage[50,63,64,71,72] and the cell growth differentiation phenomenon.[60,61,65,68,69]

2.2.1 Data treatment. The evolution of the maximal surface traction was monitored on each cell over time and identified visually by a small open circle such as represented in Fig. 3. Variations in distance $d_{i,i+1}$ between cells i and $i + 1$, cell rotation rates Ω_i, and tractions exerted at both ends of each cell were recorded and compared (i) between chains of different lengths and (ii) for all cells within a given chain.

3 Shearing impact on bacterial functionality and spatial organization of bacterial suspensions

3.1 Categories describing bacterial spatial organization

In order to standardize our observations and gather statistics, different categories were created to describe bacterial spatial organization: single cells, chains ranging from 2 to 10 cells, chains of more than 10 cells ("long chains"), and flocs. Flocs stand for (i) bacterial cells sticking together by their sides, when 3 or more cells are stuck, (ii) two or more bacterial chains close to one another bend excessively ("destructured chains" with apparent overlaps), or (iii) a mix of the two previous cases. Floc type (ii) could be caused by mechanical strain sensing leading to cell wall elongation.[73] Bacterial floc types (i) and (ii) are represented in Fig. 4. Flocs can be of various sizes, as long as all cells within a given floc remain connected to one another.

3.2 Bacterial chain size distribution

3.2.1 One-time shearing experiments. Bacterial chain size distribution has been monitored before and after shearing for the characteristic shear rates of 244 (no air pressure applied), 3.0×10^5, 3.7×10^5, 4.2×10^5, 4.9×10^5, and 11×10^5 s^{-1} for LGG WT, LGG *spaCBA*, and LGG *welE*. Results for 244, 3.0×10^5, 4.9×10^5, and 11×10^5 s^{-1} are presented in Fig. 5 for LGG WT and in Table 3 for all strains. The behavior of the double mutant LGG *welE-spaCBA* was not investigated in this section. Comprehensive data sets for all shear rates are available in ESI.†

Initially, 25% of all bacterial suspensions consisted in long chains (more than 10 cells). Flocs were the second major category, ranging from 16% (LGG *welE*) to 30% (LGG *spaCBA*). Little or no single cells were initially found, and other chain lengths appeared to be randomly distributed, with proportions ranging from 1 to 10%.

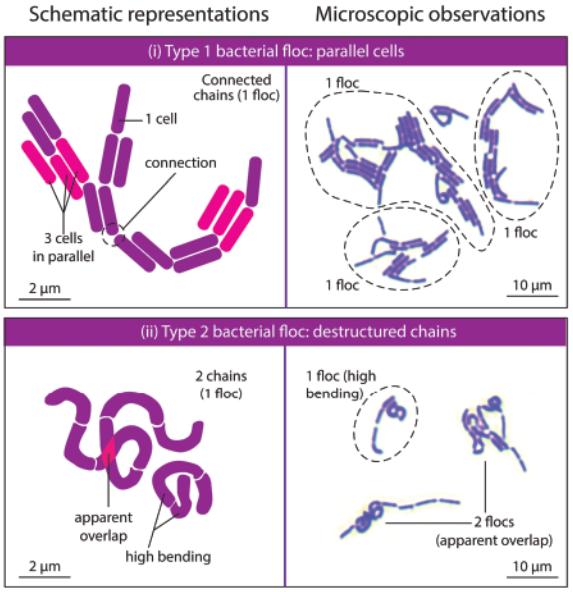

Fig. 4 Representation of bacterial flocs types: parallel bacterial cells (i) and destructured chains (ii); representative microscopic pictures of each floc type for *Lactobacillus rhamnosus* GG WT are presented to illustrate the proposed schematic representations.

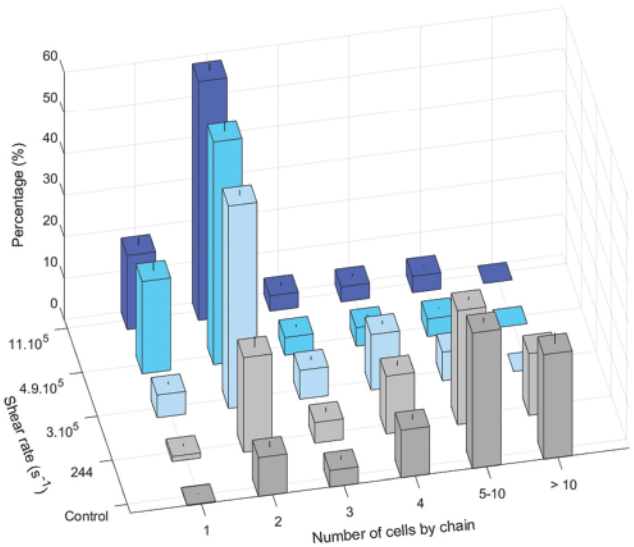

Fig. 5 Bacterial chain size distribution for the strain *Lactobacillus rhamnosus* GG "wild type" (WT) before (control) and after shearing at 244, 3.0×10^5, 4.9×10^5, and 11×10^5 s^{-1}. Error bars correspond to standard errors.

Table 3 Impact of one-time applied shear stress on bacterial chain size distribution (expressed in proportion of total number of chains and flocs) for *Lactobacillus rhamnosus* GG WT, *spaCBA*, and *welE*. Standard errors are presented for thirty measurements

Shear rate (s^{-1})	Single cells (%)	2-Cell (%)	3-Cell (%)	4-Cell (%)	5 to 10-cell (%)	>10 cells (%)	Flocs (%)
LGG WT							
Control	0 ± 0	4.8 ± 1.6	2.0 ± 1.0	12.5 ± 2.4	33.9± 1.6	23.9 ± 3.2	22.9 ± 2.2
244	0 ± 0	5.0 ± 1.4	2.2 ± 1.3	10.3 ± 2.5	34.0 ± 1.5	29.0 ± 4.7	19.6 ± 3.6
3.0×10^5	3.9 ± 1.2	56.9 ± 3.6	6.0 ± 1.5	18.9 ± 3.8	5.8 ± 0.5	0 ± 0	8.6 ± 1.8
4.9×10^5	10.7 ± 2.4	57.9 ± 3.6	5.2 ± 1.4	6.3 ± 1.7	4.0 ± 0.4	0 ± 0	15.9 ± 2.5
11×10^5	22.4 ± 1.7	55.0 ± 2.0	3.4 ± 0.5	2.6 ± 0.5	0.9 ± 0.1	0 ± 0	15.6 ± 2.0
LGG *spaCBA*							
Control	1.2 ± 0.5	6.7 ± 1.2	2.1 ± 0.6	6.2 ± 1.1	25.5 ± 1.0	26.6 ± 3.0	31.6 ± 2.7
244	1.1 ± 0.5	9.3 ± 1.1	3.2 ± 0.8	10.0 ± 1.4	25.2 ± 0.8	17.4 ± 2.0	33.8 ± 1.6
3.0×10^5	4.3 ± 0.8	34.4 ± 2.0	12.0 ± 1.6	19.5 ± 1.5	8.4 ± 0.4	0 ± 0	21.4 ± 1.4
4.9×10^5	14.6 ± 1.5	52.1 ± 1.6	7.1 ± 0.6	8.7 ± 0.8	2.8 ± 0.1	0 ± 0	14.6 ± 1.3
11×10^5	16.5 ± 1.3	47.6 ± 1.5	5.0 ± 0.4	5.8 ± 0.7	1.3 ± 0.1	0 ± 0	23.8 ± 1.2
LGG *welE*							
Control	0.18 ± 0.2	9.3 ± 1.4	4.0 ± 1.1	11.5 ± 1.3	32.7 ± 1.1	25.3 ± 2.7	16.9 ± 1.5
244 s^{-1}	1.2 ± 0.6	22.9 ± 2.6	5.0 ± 1.1	13.9 ± 1.2	27.5 ± 0.8	14.9 ± 1.4	14.5 ± 1.8
3.0×10^5	5.4 ± 0.7	48.8 ± 1.3	7.0 ± 0.9	13.3 ± 0.8	6.9 ± 0.3	0 ± 0	18.5 ± 1.0
4.9×10^5	22.2 ± 2.0	53.7 ± 2.4	4.2 ± 0.6	4.4 ± 0.6	4.3 ± 0.3	0 ± 0	13.9 ± 1.9
11×10^5	17.9 ± 1.8	58.0 ± 1.8	3.7 ± 0.7	3.6 ± 0.5	3.94 ± 0.2	0.55 ± 0.5	15.2 ± 1.5

When sheared at very low shear rate (244 s^{-1}), the chain distribution of LGG WT remained mostly similar to the control. For the two other strains, however, a significant decrease in long chains occurred (about 10%). This loss was compensated by an increased proportion of smaller chains and especially of 2-cell chains for LGG *welE* (2.5 times higher than for the control).

At low industrial air pressures (0.2 bar, *i.e.* 3.0×10^5 s^{-1}), the proportion of 2 cell-chains drastically increased, ranging from 35% for LGG *spaCBA* up to 57% for LGG WT (so 11 times higher than when no air pressure was applied). The proportion of 3 and 4-cell chains was also multiplied by 2 to 4 for LGG WT and *spaCBA* and increased to a lesser extent for LGG *welE*. In parallel, the number of chains from 5 to 10-cells was divided by 3 to 6 depending on the strain. Long chains were no longer present in suspension whichever strain, whereas single cells started appearing (about 4–5%).

At higher shear rates (4.9×10^5 and 11×10^5 s^{-1}) proportions of 3-cell and 4-cell chains kept on decreasing and single cells kept on increasing, whereas the proportion of 2-cell chains did not vary much once it has reached about 50% of the suspension. No drastic variation was observed between 4.9×10^5 s^{-1} (1 bar) and 11×10^5 s^{-1} (4 bars). Eventually, single cells represented 15–20% of the final suspension, 2-cell chains 50–60%, and longer chains less than 15%.

The strain LGG *spaCBA* was less impacted by chain breakage at low air pressures, as 2-cell chains represented only 35% of its total chain distribution, *versus* 50% or more for the two other strains. Concomitantly, LGG *spaCBA* was also identified as the strain the most likely to flocculate (Table 3). Therefore, it can be suggested that flocs may help preserving bacterial chains from breaking. However, it was difficult to estimate to which extent floc breakage played a role, as flocculation may also result from the fixation of bacterial cells onto a surface thus not necessarily being representative of what occurs in suspension.

Overall, most breakage events occurred at low air pressures and led to a drastic increase in 2-cell chains, which seem to be the major and most stable form of bacterial chains in flow. Indeed, this form is able to resist even shear rates as high as 11×10^5 s^{-1} without breaking. Higher shear rates than 3.0×10^5 s^{-1}, although not inducing such drastic changes, generated additional strain-dependent bacterial chain breakage and led to an increased proportion of single cells.

A hypothesis for why 2-cell chains appear to be the most favorable configuration under shear could be that forces exerted on

Table 4 Impact of repeated shear stress ('repeat') compared to one-time shear stress ('one-time') at high shear rate (11×10^5 s^{-1}) on bacterial chain distribution (expressed in proportion of total number of chains and flocs) for *Lactobacillus rhamnosus* GG, *spaCBA*, and *welE*. Initial chain distributions are used as controls. Standard errors are presented for thirty measurements; for each strain, different letters a–c within the same row attest of statistically significant differences

	LGG WT			LGG *spaCBA*			LGG *welE*		
	Control (%)	One-time (%)	Repeat (%)	Control (%)	One-time (%)	Repeat (%)	Control (%)	One-time (%)	Repeat (%)
Single cells	0.0 ± 0.0^a	$22 \pm ^b$	38 ± 2^c	1.2 ± 0.5^a	16 ± 1^b	36 ± 1^c	0.2 ± 0.2^a	18 ± 2^b	52 ± 2^c
2-Cell chains	4.8 ± 1.5^a	55 ± 2^b	47 ± 2^b	6.7 ± 1.2^a	48 ± 2^b	43 ± 1^b	9.3 ± 1.3^a	58 ± 2^b	33 ± 2^c
3-Cell chains	2.0 ± 1.0^a	3.4 ± 0.5^b	1.4 ± 0.4^a	2.1 ± 0.6^a	5.0 ± 0.4^b	3.4 ± 0.3^c	4.0 ± 1.1^a	3.7 ± 0.7^a	2.9 ± 0.9^a
4-Cell chains	12 ± 2^a	2.6 ± 0.5^b	1.6 ± 0.4^b	6.2 ± 1.1^a	5.8 ± 0.7^a	1.7 ± 0.3^b	11 ± 1^a	3.6 ± 0.6^b	0.3 ± 0.2^c
Flocs	23 ± 2^a	16 ± 2^b	11 ± 2^b	32 ± 3^a	24 ± 1^b	16 ± 1^c	17 ± 2^a	15 ± 2^{ab}	11 ± 1^b

the cells of 2-cell chains are minimized compared to other forms. This hypothesis will be furthered explored in the modeling part. Four-cell chains are the second major and most stable form, especially at low and intermediate air pressures (0.2 and 1 bar *i.e.* 3.0×10^5 and 4.9×10^5 s^{-1}). This may suggest a breakage mechanism in three pieces, two single cells and one 2-cell chain. This hypothesis will also be furthered discussed in the modeling part.

3.2.2 Repeated *versus* one-time shearing. The effect of repeated *versus* one-time shearing on bacterial chain size distribution is presented in Table 4 for LGG WT, *spaCBA*, and *welE* for the highest shear rate (11×10^5 s^{-1}). Only impacted bacterial chain categories are presented in Table 4. Comprehensive data sets are available in ESI.†

Repeated shearing reduced the proportions of all kind of chains and flocs and increased the proportion of single cells for all strains. However, this impact also appeared both strain- and chain length-dependent. More than 50% of the final LGG *welE* suspension consisted in single cells *versus* 35–40% for the two other strains. Proportion of 2-cell chains also decreased by a third for LGG *welE* whereas a slighter decrease (not significant) was observed for LGG WT and *spaCBA*. Finally, for LGG *welE* the proportion of 4-cell chains was divided by a factor of 10 for repeated *versus* one-time shearing whereas it was only divided by 2 for LGG WT and by 3 for LGG *spaCBA*. LGG *welE* therefore appeared more sensitive to repeated shearing than the two other strains.

Three-cell and 4-cell chains appeared to be more sensitive to repeated shearing than 2-cell chains and flocs, especially for LGG WT and *spaCBA*. They would therefore be more likely the cause of the single cells increase evidenced at high shear rates.

Overall, the two main effects of repeated *versus* one-time shearing seemed to be (i) doubling the single cells proportion for all strains and (ii) decreasing the 2-cell chains proportion (up to a third for LGG *welE*).

Two hypotheses can be formulated to explain the fact that LGG *welE* was found to be the most shearing-sensitive strain. On one hand, as this strain is impaired in EPS production, connections between cells within a chain are less protected from shearing. EPS could also play a protective role on the way shearing constraints apply to the cells, by increasing the fluid viscosity for example.[74] However, this hypothesis does not explain the chain length dependency. On the other hand, LGG *welE* is expected to be the most adhesive of the three investigated strains due to its increased pili exposure.[24,53] This could have resulted in a higher degree of adhesion to the walls of the nozzle. As bacteria attached to walls would be likely to undergo a higher shearing stress under flow, LGG *welE* would be more affected by shearing and its chains therefore more easily broken. It could also be envisioned that proximity to the walls may be favored for some chain types depending on their length and weight. Differential distribution of cells across a channel section due to weight differences was indeed previously observed for blood cells in a shear flow.[75,76] It was identified as a major factor leading to differential adhesion to channel walls.[76,77]

3.3 Bacterial functionality

The impact of shearing on bacterial adhesive abilities was evaluated for shear rates ranging from 244 to 11×10^5 s^{-1} for all four LGG strains *i.e.* WT, *spaCBA*, *welE*, and D2 (*welE-spaCBA*). Results are presented in Table 5.

Observed impacts were strain-dependent. Indeed, the highest functionality losses observed for one-time-applied shearing ranged from 1% (LGG WT) to more than 30% for LGG *welE*. Surprisingly, in the case of the strain featuring the lowest adhesive abilities, LGG *spaCBA*, shearing seemed to increase adhesive abilities (marked as "negative adhesion losses" in Table 5).

The adhesive abilities of LGG WT were the least affected by shearing. One-time shearing indeed did not significantly impact this strain's adhesive abilities. Even when applying the highest shear rate repeatedly, losses remained inferior to 20%. However, for higher shear rates such as those applied during spray-drying by Kiekens *et al.* on the same strain (using an air flow rate $\dot{q}_A$ five times higher than the highest value of $\dot{q}_A$ used in the current study), LGG WT was imaged without pili after shearing and functionality losses went over 70% when evaluated as the ability to adhere to Caco-2 cells.[29] This drastic decrease found in previous literature can look surprising in regard to our results. Three hypotheses can be made to explain this difference: (i) different surface molecules are involved in adhesion to β-lactoglobulin compared to Caco-2 cells and the first may be less shear-sensitive than the second, (ii) there is a shear rate threshold below which bacterial surface is little

Table 5 Impact of shearing on bacterial adhesive abilities of LGG WT and the three mutant strains LGG *spaCBA*, *welE*, and D2 (*welE-spaCBA*). Standard deviations have been calculated. All values of $1000/t_{start}$ have been normalized with the control, using the adhesion of LGG WT to β-lactoglobulin. Loss percentages have been normalized with the control by strain. Different letters a–d within the same column attest of statistically significant differences

	LGG WT		LGG *spaCBA*		LGG *welE*		LGG D2	
$\dot{\gamma}$ (10^5 s^{-1})	$1000/t_{start}$	Loss (%)	$1000/t_{start}$	Loss (%)	$1000/t_{start}$	Loss (%)	$1000/t_{start}$	Loss (%)
Control	1.01 ± 0.09^a	0	0.41 ± 0.050^a	0	1.8 ± 0.09^a	0	0.77 ± 0.11^a	0
0.00244	1.05 ± 0.14^a	−1	0.41 ± 0.038^a	0.5	1.5 ± 0.06^b	17	0.70 ± 0.049^b	9
3.0	1.03 ± 0.16^a	−5	0.50 ± 0.067^b	−22	1.6 ± 0.04^b	11	0.71 ± 0.063^a	8
3.7	1.06 ± 0.13^a	−3	0.49 ± 0.057^b	−19	1.4 ± 0.03^{bc}	19	0.73 ± 0.083^a	5
4.2	1.02 ± 0.15^a	−6	0.49 ± 0.057^b	−20	1.4 ± 0.02^{bc}	18	0.72 ± 0.062^a	6
4.9	1.00 ± 0.14^a	−2	0.49 ± 0.056^b	−19	1.4 ± 0.02^{bc}	22	0.69 ± 0.054^b	10
11 (one-time)	0.99 ± 0.16^a	1	0.48 ± 0.048^b	−18	1.2 ± 0.05^c	31	0.67 ± 0.069^b	13
11 (repeated)	0.86 ± 0.020^a	14	0.43 ± 0.0090^{ab}	−5	0.78 ± 0.016^d	56	0.57 ± 0.010^b	26

affected but can be almost completely "shaved" once past it, or (iii) other kinds of stresses, such as heat stress and osmotic stress (spray-drying and rehydration) may have come into play and, combined with shearing, may have had a lot more impact on bacterial surface.

The adhesive abilities of the pili-depleted strain LGG *spaCBA* increased by 20% when the suspension was sheared once even for very low air pressures (0.2 bar *i.e.* 3×10^5 s^{-1}). However, when the highest shear rate was repeatedly applied, cells in both sheared and control suspensions presented similar adhesive abilities. This could be explained by partial removal of the EPS surface layer upon shearing, which would expose other adhesive surface proteins.[53] This is supported by the fact that the double mutant strain LGG D2 (pili- and EPS-depleted) was found to have an adhesive capacity superior to LGG *spaCBA* in control conditions, which could be due to the presence of other adhesive proteins on the cell surface (usually buried in the EPS layer). Another recent study attests of the impact of shearing on the mechanical breakdown of EPS molecules[78] that could reveal underlying proteins. The existence of such adhesive surface proteins hidden within the EPS layer has previously been pointed out.[25,79,80] Potential candidates that could mediate adhesion in the absence of pili include the Mucus Binding Factor MBF, the MbA protein, lipoteichoïc acids or peptidoglycans, all being present on LGG cell surfaces and buried within the EPS layer.[25,53] The EPS themselves have previously been found to play a positive role in adhesion, although of less importance than the role played by pili.[53] Shearing could therefore be seen as a positive step for low-adhesive strains, possibly allowing them to reveal their adhesive potential.

LGG D2 presented adhesive abilities losses at high shear rates (up to 13% for one-time applied shearing), suggesting that the other surface proteins contributing to bacterial adhesion may also get damaged by shearing. On the contrary, LGG *spaCBA* adhesive abilities were always increased by shearing, the lowest increase resulting from repeated shearing. A hypothesis could be that, in the range of investigated shear stresses, the EPS layer of LGG *spaCBA* could not be completely removed after one-time shearing, and that the remaining parts of this layer may surround and therefore "protect" the other underlying adhesive surface proteins. Less forces were therefore exerted on these more buried sites, which are thus more preserved and could later act as adhesive patches. However, under repeated shearing, the EPS of LGG *spaCBA* would be more completely removed and therefore the underlying surface adhesive molecules more damaged, leading to a smaller gain in adhesive abilities.

Initially the most adhesive strain, LGG *welE* was also the most impacted by shearing. Losses gradually increased with increasing shear rate. For shear rates from 3.0×10^5 to 4.9×10^5 s^{-1} they approached 20% whereas for the highest shear rate they reached respectively 31% and 56% for one-time *vs.* repeatedly applied shearing. The fact that LGG *welE* is a lot more sensitive to shearing than LGG WT may be due to the fact that pili would be partially protected by the EPS layer featured by LGG WT, which could prevent their removal and limit the forces exerted at the pili basis. EPS have indeed recently been shown to feature a protective effect against shearing in terms of bacterial functionality for *Lactococcus lactis* subsp. *cremoris* in fermented milk compared to non-EPS-producing strains.[81] The full pili-exposure of LGG *welE*, presented in previous studies as a competitive advantage allowing higher adhesive abilities,[24,52,82] revealed here to be a competitive disadvantage in shearing environments.

It can also be noticed that even after repeated shearing at the highest shear rate, strains still presented significant adhesive abilities differences. This suggests that each strain possesses a minimal adhesion level below which it does not seem possible to get. However, the classification of strains according to their adhesive abilities is changed by repeated shearing. Before shearing, adhesive abilities were stronger such as LGG *welE* > LGG > LGG WT > LGG D2 > LGG *spaCBA* whereas after shearing, LGG WT > LGG *welE* > LGG D2 > LGG *spaCBA*. This suggests that the wild type strain is the best adapted to stressful environmental changes. Further experimental research may focus on shear-induced changes on LGG cell surfaces to confirm the hypotheses on the roles under shear of the different cell wall components. Such research could be performed using advanced microscopy techniques, such as atomic force microscopy or transmission electron microscopy.

4 Modeling shear flow impact on bacterial chain integrity

Considering that the major shearing impact both in terms of adhesive abilities losses and chain breakage occurred at the lowest air pressure (0.2 bar, *i.e.* 3.0×10^5 s^{-1}), we wondered whether these two phenomena could be correlated and why this impact was little changed by higher shear rate values. By proposing a model dealing with mechanical forces applied individually to each cell in a chain, we thought a rationale may emerge that could explain qualitatively the collective behavior observed experimentally at the level of the suspension. This section focuses on the impact of shearing on bacterial chains integrity at the cell scale by answering one central question: do bacterial chains matter in a shear flow in terms of bacterial functionality?

This question will be investigated by looking at the influence of (i) the position of a body within a chain, (ii) the chain angle with the horizontal during a chain rotation period, and (iii) chain length on bacterial adhesive surface proteins (ASP) removal, such as pili and small filamentous adhesive proteins.

4.1 Bacterial adhesive surface proteins removal and their relationship to surface traction

In this section we seek to justify the use of surface traction as a proxy for pili removal rate, or more generally, ASP removal rate. To address this issue we first determine the traction on the surface of a spherical cell body in a background shear flow in three different scenarii: (i) the body undergoes free translation/rotation in the flow, (ii) the body is fixed in space, and (iii) the body is part of a bacterial chain which is freely moving in the

flow. Then, we will determine the viscous force applied to a pilus fixed on a given cell of a bacterial chain in a shear flow and compare it to the traction force expressions previously established.

4.1.1 Traction on a lone, freely-moving spherical cell. Consider a background shear flow $\boldsymbol{u}^\infty = \dot{\gamma} y \hat{\boldsymbol{x}}$ and a sphere with center at $\boldsymbol{x}_0 = x_0\hat{\boldsymbol{x}} + y_0\hat{\boldsymbol{y}}$. We will consider the possibilities that the sphere is held in the flow with force $\boldsymbol{F}$ and torque $\boldsymbol{L}$, or free to move with the flow in a force- and torque-free manner. The velocity field due to the presence of the sphere at a point $\boldsymbol{x} = (x,y,z)$ in the flow is given by

$$\boldsymbol{u}(\boldsymbol{x}) = \boldsymbol{u}^\infty(\boldsymbol{x}) + \frac{1}{8\pi\mu}\left(1 + \frac{a^2}{6}\nabla^2\right)\boldsymbol{G}(\boldsymbol{x}-\boldsymbol{x}_0)\cdot\boldsymbol{F} + \frac{1}{8\pi\mu}\boldsymbol{G}^c(\boldsymbol{r}(s)-\boldsymbol{x}_0)\cdot\boldsymbol{L} + \left(1 + \frac{a^2}{10}\nabla^2\right)\nabla\boldsymbol{G}(\boldsymbol{r}(s)-\boldsymbol{x}_0):\boldsymbol{S}, \tag{9}$$

where $\boldsymbol{G}_{ij}(\boldsymbol{r}) = \delta_{ij}/r + r_i r_j/r^3$ is the Stokeslet singularity, with $r = |\boldsymbol{r}|$, $\boldsymbol{G}^c_{ij}(\boldsymbol{r}) = \varepsilon_{ijk}r_k/r^3$ is the rotlet, and the coefficient matrix $\boldsymbol{S}$ itself is often referred to as the stresslet. Generically, with $\boldsymbol{U}$ and $\boldsymbol{\Omega}$ the translation and rotation rate of the sphere, we have Faxén's Laws (see ref. 83), $\boldsymbol{F} = 6\pi\mu a(\boldsymbol{U} - \boldsymbol{u}^\infty(\boldsymbol{x}_0))$, $\boldsymbol{L} = 4\pi\mu a^3(2\boldsymbol{\Omega} - \nabla\times\boldsymbol{u}^\infty(\boldsymbol{x}_0))$, and $\boldsymbol{S} = (20\pi\mu a^3/3)\boldsymbol{E}^\infty$, where $\boldsymbol{E}^\infty = (\dot{\gamma}/2)(\hat{\boldsymbol{x}}\hat{\boldsymbol{y}} + \hat{\boldsymbol{y}}\hat{\boldsymbol{x}})$ is the symmetric rate-of-strain tensor describing the background flow. The associated traction is given by (with $\boldsymbol{x} \in \boldsymbol{D}$, the surface of the sphere),

$$\boldsymbol{f}(\boldsymbol{x}) = -\frac{1}{4\pi a^2}\boldsymbol{F} - \frac{3}{8\pi a^4}\boldsymbol{T}\times\boldsymbol{x} + \frac{5\mu}{a}\boldsymbol{E}^\infty\cdot\boldsymbol{x}. \tag{10}$$

If the sphere is free to rotate in the flow, then $\boldsymbol{U} = \boldsymbol{u}^\infty(\boldsymbol{x}_0)$ and $\boldsymbol{\Omega} = \nabla\times\boldsymbol{u}^\infty(\boldsymbol{x}_0)/2$ (and the body is force and torque free), so the traction is

$$\boldsymbol{f}(\boldsymbol{x}) = \frac{5\dot{\gamma}\mu}{2a}((y-y_0)\hat{\boldsymbol{x}} + (x-x_0)\hat{\boldsymbol{y}}), \tag{11}$$

which is notably independent of the sphere size.

We denote by Max_f the maximal surface traction over a given cell body; on cell body q we have $\mathrm{Max}_f = \| |\mathbf{f}_q| \|_\infty = \max_{\mathbf{x}\in D_q}|\mathbf{f}|$. In the case above we have $\mathrm{Max}_f = 5\dot{\gamma}\mu/2$.

4.1.2 Traction on a fixed spherical cell. From eqn (10), if the spherical cell is held fixed in the flow, then $\boldsymbol{U} = \boldsymbol{\Omega} = 0$, resulting in the traction distribution

$$\boldsymbol{f}(\boldsymbol{x}) = \frac{\dot{\gamma}\mu}{2a}[(3y_0 + 8(y-y_0))\hat{\boldsymbol{x}} + 2(x-x_0)\hat{\boldsymbol{y}}]. \tag{12}$$

The maximal surface traction is now $\mathrm{Max}_f = (\dot{\gamma}\mu/2)|8 + 3y_0/a|$. If the sphere is centrally located at $y_0 = 0$, then the traction remains independent of the size; it is larger than that for a freely moving sphere but only by a factor of 8/5. This is because the boundary conditions are naturally not satisfied by a fixed sphere without disturbing the background flow, but this is also true of a rotating sphere with nearly identical consequences.

If the sphere is held in the oncoming flow, however, with $y_0 \neq 0$, the traction now depends on the size of the sphere, with smaller spheres experiencing larger tractions, inversely proportional to the radius a (the viscous force on the body scales linearly with a, and distributing the force over the surface area results in division by a^2; see ref. 83).

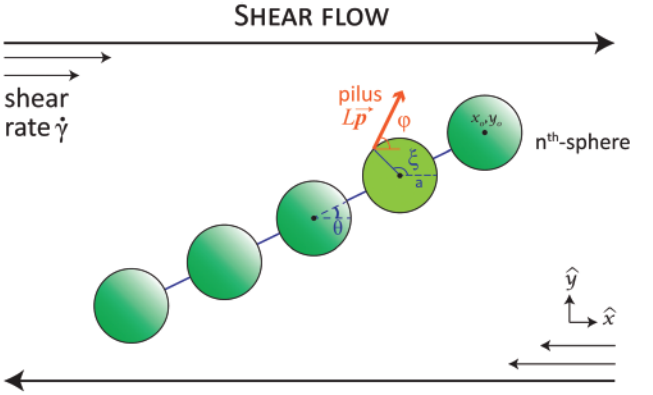

Fig. 6 Schematic of the pilus on a body in the chain. Only one pilus has been represented for better readability of the figure. n is measured from the center of the chain. The pilus has length L and points in the $\hat{\boldsymbol{p}}$ direction. The chain makes an angle θ with the horizontal. Chain motion is assumed here to be rigid.

4.1.3 Traction on a spherical cell in a chain. One way for a cell to be "held in the flow" in a transient sense is if it is part of a chain of bodies, which rotates as a whole with zero net force and torque. Using the simplest resistive force theory to describe the motion of a chain of bodies (*i.e.* neglecting the hydrodynamic interactions among the bodies), we find that the rotation rate is $\boldsymbol{\Omega} = -\dot{\gamma}/2(1 - \cos(2\theta))\hat{\boldsymbol{z}}$ (see also ref. 84), where θ is the orientation angle relative to $\hat{\boldsymbol{x}}$, such as presented in Fig. 6. Associated with this rotation, with the chain centered at the origin, the nth sphere away from the origin moves with speed $\boldsymbol{U} = \boldsymbol{\Omega}\times[na(\cos\theta\hat{\boldsymbol{x}} + \sin\theta\hat{\boldsymbol{y}})] = a\dot{\gamma}n\sin^2\theta(\sin\theta\hat{\boldsymbol{x}} - \cos\theta\hat{\boldsymbol{y}})$, and rotates with rate $\boldsymbol{\Omega}$, resulting in a traction (which neglects hydrodynamic interactions among the bodies),

$$\boldsymbol{f}(\boldsymbol{x}) = \frac{\dot{\gamma}\mu}{2a}(3an\sin\theta\cos^2\theta + (5 + 3\cos(2\theta))(y-y_0))\hat{\boldsymbol{x}} + \frac{\dot{\gamma}\mu}{2a}(3an\sin^2\theta\cos\theta + (5 - 3\cos(2\theta))(x-x_0))\hat{\boldsymbol{y}}, \tag{13}$$

where $\boldsymbol{x}_0 = an(\cos\theta\hat{\boldsymbol{x}} + \sin\theta\hat{\boldsymbol{y}})$. Since $|\boldsymbol{x} - \boldsymbol{x}_0| = a$ we observe that the traction is again independent of a. However, it increases linearly with n, the position along the chain. Here we find $\mathrm{Max}_f = (5\dot{\gamma}\mu/2)|1 + 3n/10|$. The traction on the nth sphere away from the center is now a factor of $1 + 3n/10$ larger than that of a freely moving sphere. In this sense, the traction on a body far from the center might be considerably reduced by abandoning the chain.

4.1.4 Relationship between adhesive surface protein removal and surface tractions. It is simpler to analyze and compute the traction on the surface of a bacterium in a flow than to study the forces on individual small ASP attached to the cell body. This raises the question: to what extent can the surface tractions described in eqn (11)–(13) be used as proxies to understand the viscous force on the ASP? The surface traction is proportional to the velocity gradient, which we expect to be

relevant to the force on the ASP. If the ASP is small relative to the body size, then the no-slip boundary condition on the cell body is particularly relevant, as it renders the fluid motionless there relative to the body motion. So the velocity of the base of the ASP is given by $\boldsymbol{U}+\boldsymbol{\Omega}\times(\boldsymbol{X}-\boldsymbol{x}_0)$, where $\boldsymbol{X}$ is the location of the ASP connection point. To determine the viscous force on the ASP, $\boldsymbol{f}_p(s)$, a function of the arc-length $s\in[0,L]$, the resistive force approximation[83] can be used again although in a different context, writing

$$\boldsymbol{f}_p(s)=\frac{2\pi\mu}{\log(2/\varepsilon_p)}[2\boldsymbol{I}-\hat{\boldsymbol{p}}\hat{\boldsymbol{p}}]\cdot(\boldsymbol{u}(\boldsymbol{r}(s))-\boldsymbol{r}_t(s)), \tag{14}$$

where $\boldsymbol{f}_p$ is the viscous force per unit length on the ASP, ε_p is the ASP aspect ratio (radius/length, assumed small), $\hat{\boldsymbol{p}}$ is the orientation of the ASP, $\boldsymbol{r}(s)=\boldsymbol{X}+s\hat{\boldsymbol{p}}$ is the position along the ASP at arc-length s, and $\boldsymbol{r}_t(s)$ is the velocity of the ASP itself there. At this point, semi-rigidity of the ASP is assumed, in order to consider first that only slight (negligible) deformation of the ASP under flow can occur. The ASP is considered in the xy-plane, with the connection point located on the sphere at an angle ξ relative to $\hat{\boldsymbol{x}}$, and fixed at an orientation angle ϕ relative to $\hat{\boldsymbol{x}}$ (Fig. 6). With its rigid body motion, it thus moves with velocity

$$\boldsymbol{r}_t=\boldsymbol{U}+\boldsymbol{\Omega}\times(\boldsymbol{r}(s)-\boldsymbol{x}_0)=\boldsymbol{U}+\boldsymbol{\Omega}\times(\boldsymbol{X}-\boldsymbol{x}_0+s\hat{\boldsymbol{p}}). \tag{15}$$

The ASP is assumed to be short relative to the cell size, or $L\ll a$.

Looking at a spherical cell free to move in the fluid, the fluid velocity along the ASP is

$$\boldsymbol{u}(s)=\frac{a\dot{\gamma}s}{2}(\sin(\xi-\phi)\hat{\boldsymbol{x}}-\cos(\xi-\phi)\hat{\boldsymbol{y}})+O(s^2). \tag{16}$$

The force on the ASP is then:

$$\boldsymbol{F}_{\mathrm{ASP}}=\int_0^L\boldsymbol{f}_p(s)\mathrm{d}s=\frac{5\pi\mu\dot{\gamma}\cos(\xi-\phi)L}{2\log(2/\varepsilon_p)}[2\sin\xi\cos(2\xi)\hat{\boldsymbol{x}}-(\cos\xi+\cos(3\xi))\hat{\boldsymbol{y}}]+O((L/a)^2), \tag{17}$$

or at worst, $\|\boldsymbol{F}_{\mathrm{ASP}}\|_\infty\leq\frac{5\pi\mu\dot{\gamma}L}{\log(2/\varepsilon_p)}+O((L/a)^2)$.

Now considering a ASP on the nth sphere away from the origin on a chain, the fluid velocity is

$$\begin{aligned}\boldsymbol{u}(s)&=a\dot{\gamma}s\sin^2\theta[(n\sin(\theta-\phi)+\sin(\xi-\phi))\hat{\boldsymbol{x}}]\\&\quad-a\dot{\gamma}s\sin^2\theta[(n\cos(\theta-\phi)+\cos(\xi-\phi))\hat{\boldsymbol{y}}],\end{aligned} \tag{18}$$

resulting in

$$\begin{aligned}\boldsymbol{F}_{\mathrm{ASP}}&=\frac{\pi\mu\dot{\gamma}\cos(\xi-\phi)L}{2\log(2/\varepsilon_p)}[\sin\xi\cos(\xi-\phi)(-6\cos(2\theta)\\&\quad+3n\sin(2\theta)\sin(\theta-\xi)+10\cos(2\xi))\hat{\boldsymbol{x}}-\cos\xi(6\cos(2\theta)\\&\quad-3n\sin(2\theta)\sin(\theta-\xi)-10\cos(2\xi))\hat{\boldsymbol{y}}]+O((L/a)^2),\end{aligned} \tag{19}$$

or at worst, $\|\boldsymbol{F}_{\mathrm{ASP}}\|_\infty\leq\frac{\pi\mu\dot{\gamma}(2+3n/2)L}{\log(2/\varepsilon_p)}+O((L/a)^2)$.

Inserting a characteristic viscosity $\mu=10^{-3}$ Pa s, shear rate $\dot{\gamma}=10^5\ \mathrm{s}^{-1}$, ASP length $L=1$ μm, and ASP aspect ratio $\varepsilon_p=1/200$, we expect forces on the ASP on the scale of $|\boldsymbol{F}_{\mathrm{ASP}}|\approx10^5$ pN. Although forces required to remove LGG pili have not been investigated in the literature, other types of pili have been shown to withstand forces on the scale of only $\approx10^2$ pN when pulled off of a substrate.[30,85] However, the relevance of these measurements to pili removal remains unclear, and more experiments are needed. Just as with the traction on the cell body, the force acting on the ASP is larger if it is on a sphere towards the end of the chain.

Comparing the viscous force acting on the ASP to the tractions derived in the previous section, we observe the proportionality relation $\|\boldsymbol{F}_{\mathrm{ASP}}\|_\infty\sim L\log(2/\varepsilon_p)^{-1}(\mathrm{Max}_f)$, which supports our consideration of the maximal surface traction as a proxy for ASP removal rate, which we use for the remainder of the paper.

4.2 Impact of the position of bacterial cells within a chain

We now investigate numerically the impact of cell position along the chain on the maximum surface traction, Max_f. Results are presented in Fig. 7 for chains of 3, 4, and 5 cells and in Movie 1 (ESI†) for a 5-cell chain.

Regardless of the chain length considered, the minimal value of Max_f reached over a half-rotation period remains below 25% of the highest value of Max_f. This minimal force is always exerted on center cells (Fig. 7). The maximal value of Max_f, as well as the range of Max_f are respectively the highest and the largest for bacterial cells at the extremities of the chain. Therefore, the closer bacterial cells are to the center of a chain, the more likely they are to be protected from damaging forces.

4.3 Impact of instantaneous chain orientation

Fig. 8 shows the evolution of Max_f by cell over one tumbling period (Max_f being periodic of period π) for the outer cells (left and right of the chain) and the center cell of a 3-cell chain. The location of the maximal traction on each body is indicated by a small open circle. Behaviors observed in Fig. 8 for outer and inner cells in 3-cell chains are similar to those of 4-cell chains and therefore have not been represented here. Complete data sets are available in ESI.†

Inner cells experience a maximal surface traction when the chain is perpendicular to the flow ($\theta=\pi/2$). This intensity remains small compared to the one experienced by outer cells, but in fact owing to the flow created by the moving outer cells is also smaller than the traction on a lone cell (Fig. 10a$_2$). Although the inner cells are in this way protected, they also experience higher internal tension in other parts of the orbit in order to maintain quasi-rigid body motion.[86] This internal tension would be responsible for the rapid decay of the distortions (much faster than the chain rotation) that can be observed on Fig. 10b$_3$ such as previously observed by Hinch.[87] This translates into higher stretching of the connections nearest to the center of the chain, such as presented in Fig. 9.

Outer cells experience two maximal tractions right before and just after the chain is perpendicular to the flow (Fig. 8).

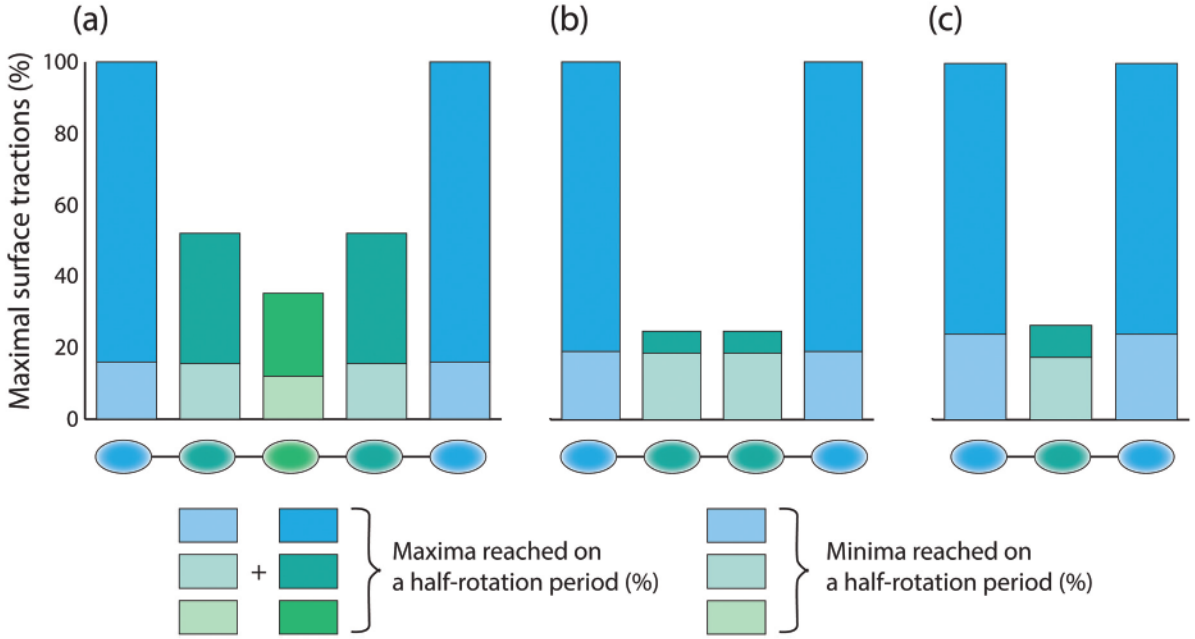

Fig. 7 Maximum surface traction forces exerted on each bacterial cell (ellipsoid body) for 5-cell chains (a), 4-cell chains (b), and 3-cell chains (c). Each bar matches the cell position represented below. Results are normalized by chain length on the highest value reached over one rotation period. Minimal values (light colors) and maximal values (sum of light colors and dark colors) reached over one rotation period are represented. Dark colors represent the range of values between which the maximum surface traction varies over one period for a given cell position in a chain.

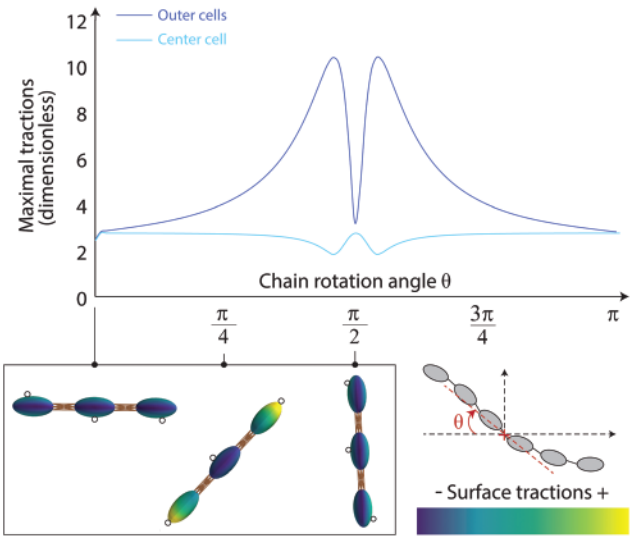

Fig. 8 Maximum surface tractions (Max_f) experienced by each bacterial cell within a 3-cell chain in a shear flow as a function of the chain rotation angle θ during a quarter rotation period; θ is the angle defined by the direction of the major axis of the central cell for odd-numbered chains, or the average major axis direction of the two inner most cells for even-numbered chains. Small open circles on pictures represent the location of the Max_f on each cell for a given θ. The full hydrodynamic color scale for surface tractions is reset every time step.

These maxima are located near the free ends (cell poles) of the outer cells which are the regions of bacterial cells that feature the most pili.[21,28] At these times, the traction reaches a minimum for the inner cells. This supports the previous hypothesis of a local environment created by outer cells in flow which would protect inner cells from the exterior shear flow. When the chain is perpendicular to the direction of flow the traction very suddenly (but momentarily) relaxes (see Movie 1, ESI† for the case of 5-cell chains). At this moment the outer cells offer minimal resistance to the flow, and the disturbance flow they create which protects the inner cells briefly vanishes (exposing the inner cells to a slightly larger traction).

Overall, bacterial cells in the interior of a chain are protected from surface tractions, but experience higher internal tension forces.[86,87] Bacterial cells at the extremities of a bacterial chain, meanwhile, experience higher surface tractions during chain tumbling, and the highest surface tractions are located near the poles, where pili are the most abundant.

4.4 Impact of bacterial chain length

The impact of chain length on maximal surface tractions exerted on individual bacterial cells within a chain in a shear flow has been investigated. Traction profiles are presented for chains of 2 up to 5 cells over a half-rotation period in Fig. 10a_1 and b_1 for outer cells, and in Fig. 10a_2 and b_2 for inner cells; the data are compared with those obtained for a single, lone cell. The case of 5-cell chains, undergoing the most deformation, is represented separately in Fig. 10b_1–b_3 as well as in Movie 1 (ESI†).

The behavior of the 5-cell chain is closer to the one described by Hinch for flexible, inextensible threads in a shear flow[87] than to buckling behaviors described by Tornberg & Shelley,[86] due to the large bending stiffness relative to stretching cost provided by the wide spring cluster (see also ref. 88 and 89).

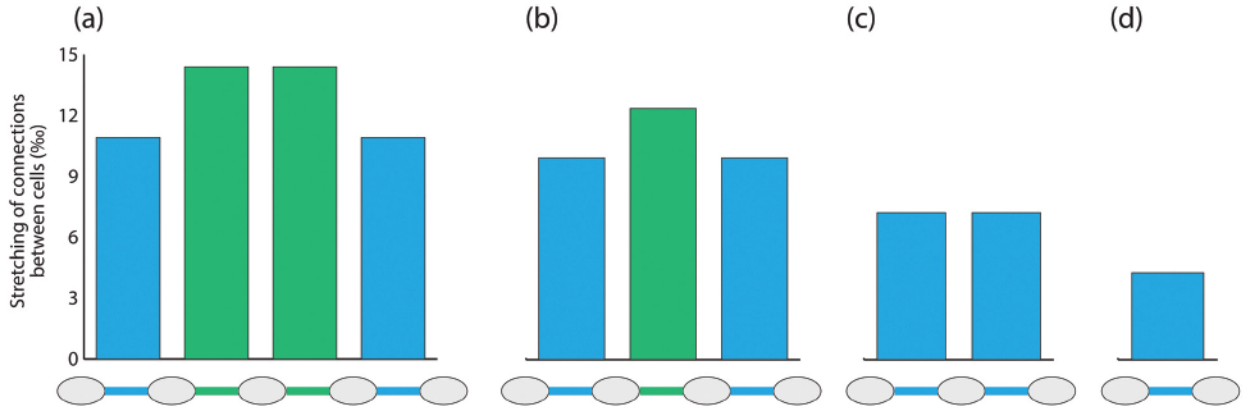

Fig. 9 Stretching of connections (cluster of springs) between bacterial cells in 5-cell (a), 4-cell (b), 3-cell (c), and 2-cell (d) chains. Values are expressed in of the resting length d of each connection, which in the model is a dimensionless constant fixed to 1. Each bar matches the connection represented below.

We will denote by FO the forces Max_f applied on the outer cells of a chain (cells at both ends of a chain), and FI the forces Max_f applied on the inner cells of a chain (all other cells, including the cell at the center of the chain).

4.4.1 Impact on outer cells. In our simulations we observed that the maximum traction on the outer cells, FO, increased monotonically as a function of chain length (Fig. 10a_1 and b_1), as predicted by eqn (17). Therefore, that the longer the chain, the more likely outer cells are to become damaged. Highest FO are reached for all chains from 2 to 5 cells right before and just after snapping through the vertical orientation. The longer the chain, the more rapid the rotation through this orientation and the closer to $\theta = \pi/2$ when highest FO are reached (Fig. 10a_1, a_3, b_1 and b_3).

When the highest maximal tractions on the outer cells are experienced, once again it is the poles of those cells that are most affected (Fig. 10a_3), which may cause important damage to adhesive surface proteins such as pili. In the case of 5-cell chains presented in Fig. 10b_1–b_3, an asymmetric behavior is observed when comparing FO before and after snapping (Movie 1, ESI†). This is due to the higher flexibility of this chain compared to the others (Fig. 10b_3). For longer chains, an S-shape deformation before and during snapping is observed, as the chain visits higher flow rates at its extremities (Fig. 10b_3(1), (2), Movie 1, ESI†). After $\theta = \pi/2$ the chain suddenly straightens (Fig. 10b_3(3)), which leads to increased FO and internal tension due to the stretching of the connections. Upon increasing the individual spring stiffness, k_L, the chain becomes more rigid, and FO before and after snapping become symmetric again, of value similar to the highest value observed for the case presented in Fig. 10b_1 and b_3 (stiff chain).

4.4.2 Impact on inner cells and potential link with chain breakage. The maximal traction forces on the inner cells, FI(3-cell chains) and FI(4-cell chains), were found to be inferior to FI(single cell) (Fig. 10a_2), suggesting that the chain environment may help protect the inner cells from viscous tractions. However, this was not the case anymore for 5-cell chains, as all inner cells featured FI higher than the single cell reference case (Fig. 10b_2). This is likely due to the more flexible behavior of chains longer than the 4-cell chain which can be observed in Fig. 10b_3 for 5-cell chains. Because of this higher flexibility, the local protective environment created by outer cells is diminished due to increased bending of the outside parts of the chain (Fig. 10b_3(2)). Right after the chain passes the vertical orientation, a rapid increase in FI can be observed. As the chain stiffens under tension the local protective environment of the inner cells is recovered, and FI decreases again. A similar but smaller effect is observed before snapping through the vertical orientation, softened by the higher deformation of the chain. Similar effects are found before and after snapping for 3-cell and 4-cell chains.

Overall, for relatively stiff chains, the internal cells in short chains are better protected than those in long chains. As chains become long enough to present more highly deformed configurations, outer cells become slightly less affected due to increased chain deformation, and inner cells are more likely to become damaged. Increased FI due to higher chain deformation, with the maximal traction located near the connection points between cells, may favor chain breakage near these points, that we will call "sensitive points" (SP).

4.5 A brief exploration of chain fragmentation

We now very briefly explore the dynamics and consequences of chain rupture on surface tractions; to do so we modify the computational model to break a spring connection if the individual Hookean spring force crosses a critical threshold, specifically a dimensionless value of 1. Fig. 11 shows a set of simplified simulations, capturing only viscous drag and torque on spherical cells and neglecting their hydrodynamic interactions.

For a 5-cell chain, the chain of spheres breaks into two 2-cell chains and one single cell, observed in Fig. 11. We observe a correlation between the points of maximal traction (the identified sensitive points, suggested in Fig. 10b_3) and the springs which rupture. This correlation was also observed for longer chains. Fragmentation into three parts was also observed for 6 and 7-cell chains, at least in this symmetric numerical experiment,

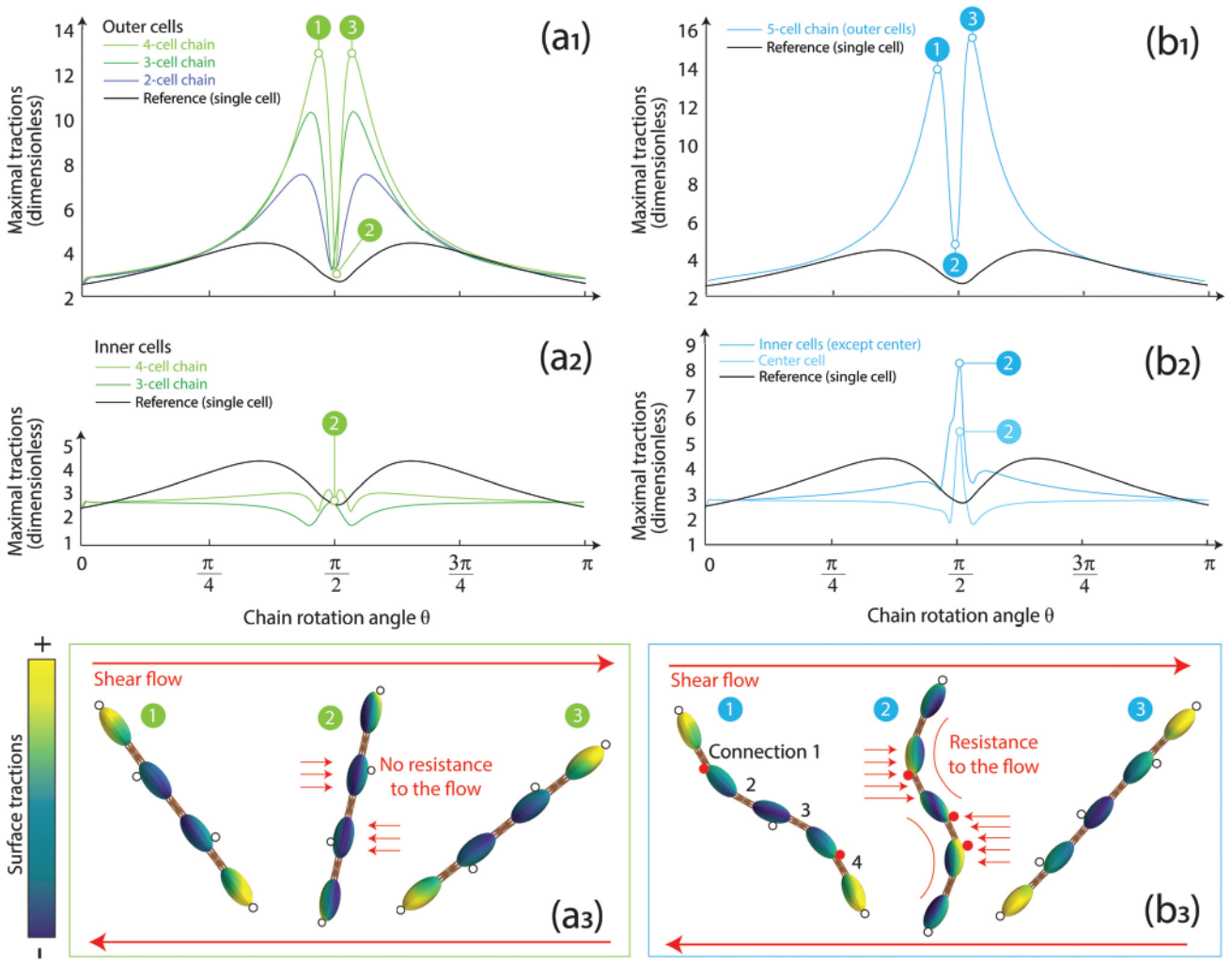

Fig. 10 Maximum surface tractions (Max_f, dimensionless) experienced by outer bacterial cells (a) and inner bacterial cells (b) of 2, 3, 4, and 5-cell chains over one period (corresponding to a half-rotation period) in quasi-rigid body motion (in the limit of the flexible regime). Model outputs are provided for maximum and minimum values of Max_f for 4-cell and 5-cell chains; small open circles and filled red dots on pictures represent the location of maximal traction for each body in a given chain configuration. Red dots stand for sensitive points (SP) identified near connection points. Results are compared with the Max_f experienced by a single cell on the same period (reference case). The full hydrodynamic color scale for surface tractions is reset every time step.

supporting the hypothesis formulated at the end of Section 3.2.1 on breakage mechanisms. This is reminiscent of the behavior of thin brittle rods submitted to excessive bending,[90] though very different physics is involved. More simulations with longer chains and involving full hydrodynamic interactions will be useful for probing the precise breaking behavior across a wider view of parameter space.

Though not presented in detail here, we also investigated breakage of 2-cell configurations (dumbbells), with hydrodynamic interactions included, to understand why this configuration seems to be the most favorable in the experiments after shearing. Testing a range of cell separation distances, d, we observed that when the connection between two dumbbell bodies is initially very short (such as what occurs soon after the cell division process), the dumbbell dynamics are roughly that of a single larger cell of higher aspect ratio, and therefore may be less likely to break. We also observed that breakage of chains occurred more readily for systems of spheres than for systems of ellipsoids. This suggests that bacterial chains composed of ellipsoidal or rod-like cells, such as lactobacilli, may be more difficult to break than chains of sphere-like cells, such as cocci.

For more flexible cases than those considered in this paper, statistical models on chain fragmentation[91–106] may also provide insight on the influence of chain length and position of bonds in the chain on the breakage phenomenon. These models make different assumptions on where chains are the most likely to break and sometime provide experimental rationales (chemical-based models correlate breakage probability with polymer weight,[95,97] energy-based models with critical bond deformation energy,[100] *etc.*). Most common modeling assumptions include mid-chain or binary breakage,[99,105] end-chain scission,[98,104] ternary breakage,[105] and random breakage.[101,105] Such theories were briefly investigated in comparison to our

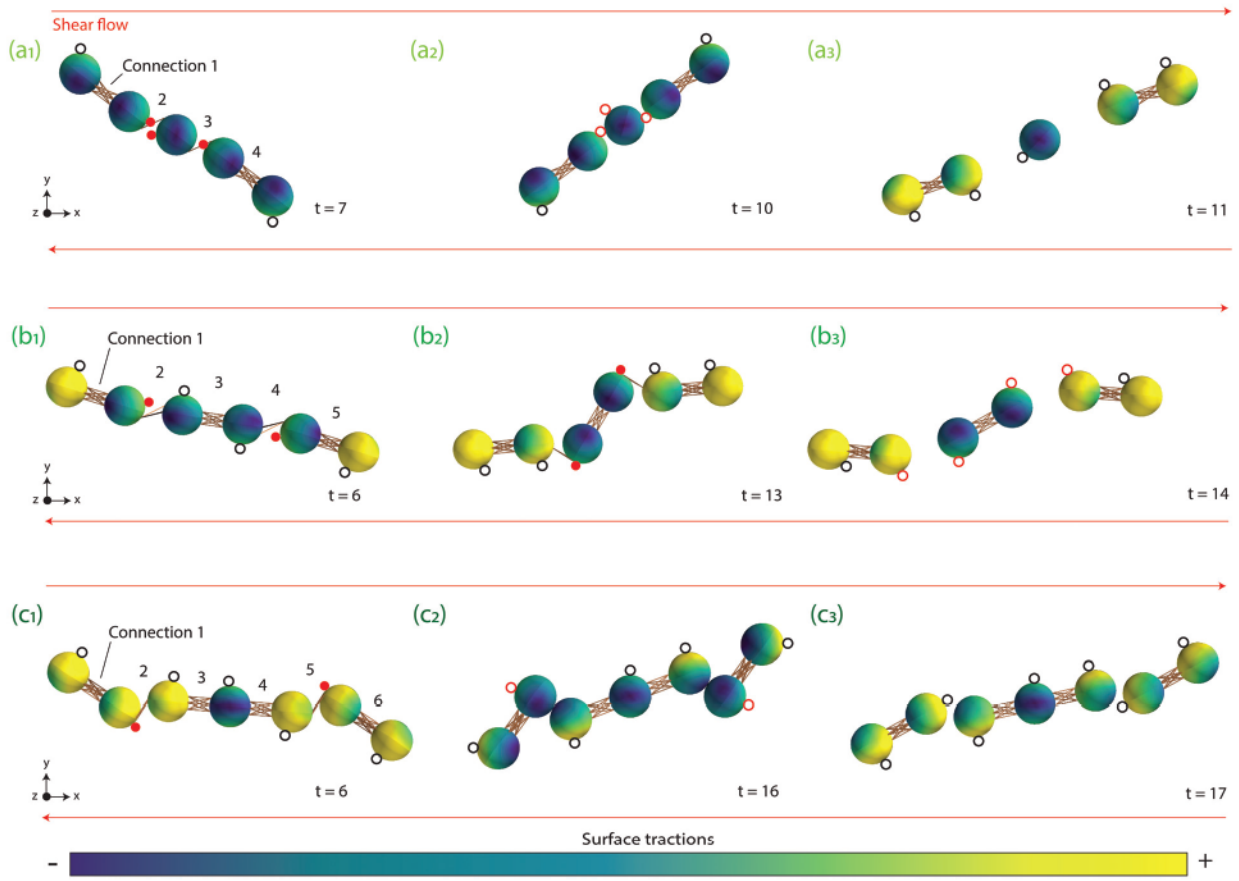

Fig. 11 Location of sensitive points (SP) on 5-cell chains (a_1–a_3), 6-cell chains (b_1–b_3), and 7-cell chains (c_1–c_3). Code was run without hydrodynamic interactions and bacterial cells were represented by spherical bodies. Open circles represent locations of maximum surface traction that do not impact connections between cells, filled red dots maximal tractions at sensitive points before breakage, and red circles maximal traction locations of previous sensitive points once connections were broken. The full hydrodynamic color scale for surface tractions is reset every time step.

experimental data by scaling the chain proportion variables on the smallest shear rate used when performing spray-drying in our experiments, *i.e.* $\dot{\gamma} = 3 \times 10^5\ s^{-1}$, but failed to provide good fits, generically leading to a much higher single-cell proportion that observed experimentally (data not shown). The fact that two-cell chains were observed to be the most stable form of bacterial chains in flow was found difficult to explain using these theoretical frameworks.

5 Conclusions

We have explored, both experimentally and by numerical simulation, the dynamics of bacterial chains in sheared environments, in the hopes to better understand the relationships between chain length, cell functionality, and a dynamic fluid environment.

In our experiments, most bacterial functionality losses and chain breakage events were observed at very low shear rates ($\dot{\gamma} = 3.0 \times 10^5\ s^{-1}$), concomitant with a rise in the proportion of 2-cell chains. As rationalized using the simulations, long chains, such as those present initially in bacterial suspensions before shearing, experience higher surface tractions than smaller chains, especially at the chain extremities. Both ends of a long chain experience high surface tractions under a shear flow, which we predict leads to "shaving" of pili and the creation of other surface damages and functionality losses.

On the contrary, cells closer to the center of the chain experience a reduced damage thanks to a local protective environment created by the outer cells, both through hydrodynamic interactions and mechanical stresses communicated by their connective matrix. As chains shorten due to breakage that we correlated with high surface tractions near sensitive points, both shear stress exerted at contact points and surface tractions exerted on cells therefore are predicted to decrease, lowering the probability of surface damage.

The upshot of our investigation is therefore that shearing-induced rupturing of bacterial chains may serve as a protective process, allowing for the preservation of bacterial functionality, such as represented in Fig. 12.

This proposed relationship between bacterial functionality and organization represents one more step towards a better understanding of the role of bacterial shape in stressful environments, and could benefit from further experimental research. The selective value of bacterial shape in relation to shear stress could for example be investigated in culture

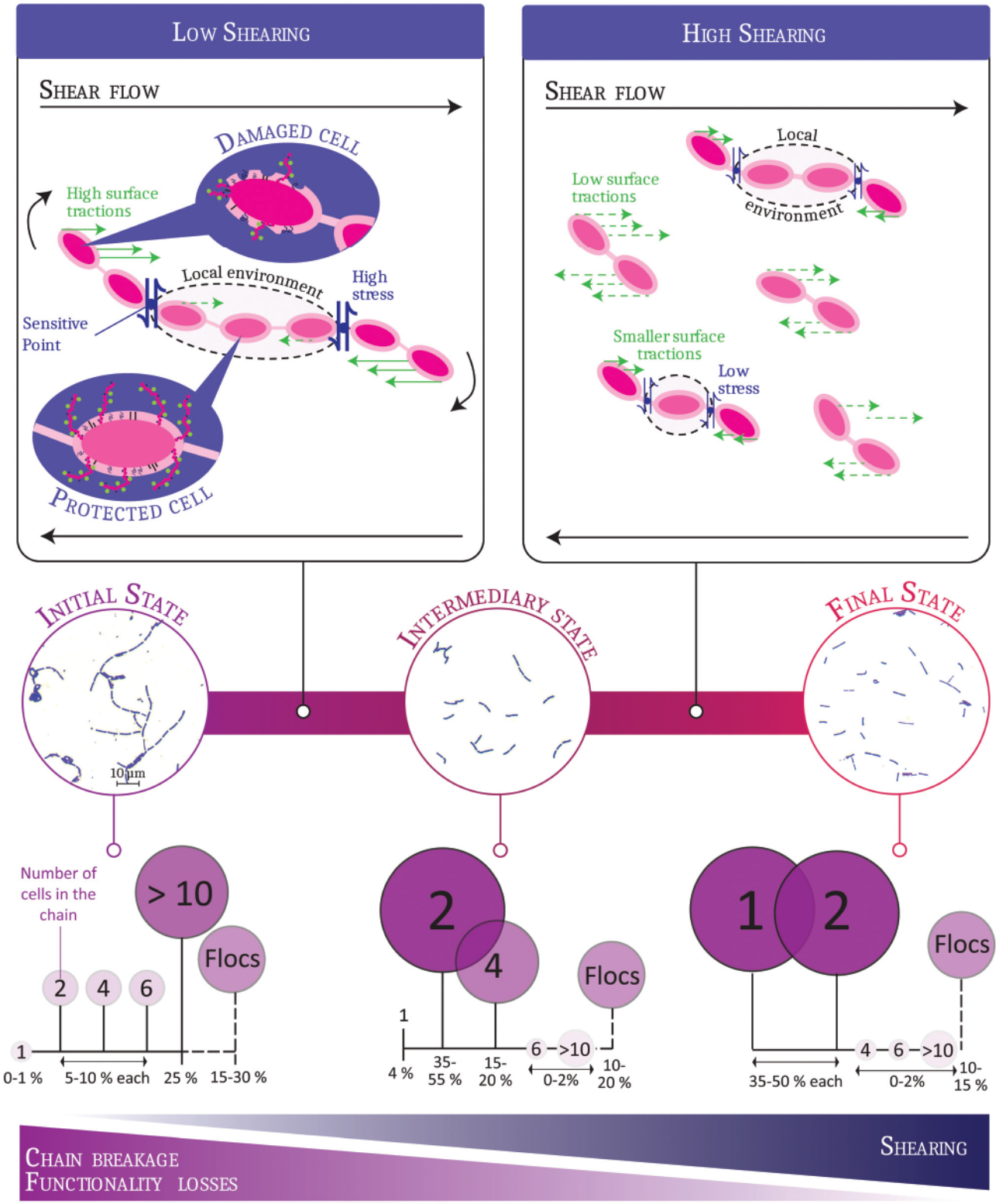

Fig. 12 Proposed relationship between bacterial functionality and shearing-induced bacterial chain breakage. Microscopic pictures illustrating the initial, intermediary, and final state have been taken for *Lactobacillus rhamnosus* GG respectively for a control suspension (initial state), after one-time shearing at a rate of $3.0 \times 10^5\ s^{-1}$ (intermediary state), and after repeated shearing at $11 \times 10^5\ s^{-1}$. Corresponding bacterial chain size distributions have been represented in percentages.

environments with local shearing constraints. This could be done by applying the methodology developed by the Lenski group that monitored the evolution dynamics over thousands of generations of *Escherichi coli* and made important discoveries on

molecular evolution and fitness gain.[107] Constraint environments could be inspired from previous studies that focused on the importance of mechanical constraints on bacterial cell shape and elongation of cell wall.[73,108]

The regioselectivity of surface traction applied to bacterial chains in a shear flow (cell position-dependency within a chain) may also play a role in bacterial evolution as it may create heterogeneity. A recent review describes the importance of microbial heterogeneity at single-cell level on population level strategies,[109] pointing out that it may play a key role in bacterial survival to unpredictable environmental changes. The cells closer to the center of a chain, more protected from stress than the outer cells, would in that sense be the ones ensuring the population's survival and renewal. Shear-induced heterogeneity could be studied further using single-cell techniques, such as suggested by recent studies.[110,111] Modification of bacterial stress sensors using reporter genes (such as fluorescent protein promoters) could allow *in situ* visualization of exerted stress on bacterial cells in a chain in a shear flow,[111] for example in microfluidic devices.

As bacterial sensitivity to shear may depend on the composition of their growing medium, the impact of protective matrices embedding bacteria such as dairy matrices on bacterial organization and functionality under shear (mimicking food manufacturing processes) may also be explored in future work.

Two other interesting future directions might include consideration of the impact of shearing when combined with other chemical parameters, such as pH, to recreate stresses experienced by bacteria during digestion, as lactobacilli may feature increased adhesive abilities after acid exposure,[112] and investigation of the role of other bacterial organization types, such as flocs, on bacterial functionality.

Author contributions

FG, SES, CG, FB conceived the research. FG, JP, WHM and SES carried out the experiments. FG, JP, and SES analyzed the data. FG and SES wrote the manuscript. All authors commented on the manuscript.

Conflicts of interest

There are no conflicts to declare.

Acknowledgements

The wild type strain LGG ATCC53103 (WT) and the derivative mutant strains *spaCBA* CMPG 5357 (impaired in pili synthesis), *welE* CMPG5351 (impaired in exopolysaccharides production), and *welE-spaCBA* CMPG5355 (double mutant), were kindly provided by Dr Sarah Lebeer (Centre of Microbial and Plant Genetics, K.U. Leuven, Leuven, Belgium, and Department of Bioscience Engineering, University of Antwerp, Antwerp, Belgium). This article has been written as part of a LUE project (Lorraine Université d'Excellence) and benefitted from a Fulbright grant. The authors would like to thank both the LUE initiative and the French-American Fulbright commission for having provided fundings and supported this work. SES acknowledges support from NSF/NIH (DMS-1661900) and the Simons Foundation's Flatiron Institute.

References

1 F. J. Carr, D. Chill and N. Maida, *Crit. Rev. Microbiol.*, 2002, **28**, 281–370.
2 K. Khalid, *et al.*, *Int. J. Biosci.*, 2011, **1**, 1–13.
3 S. A. Hayek and S. A. Ibrahim, *Food Nutr. Sci.*, 2013, **4**, 73–87.
4 E. J. Quinto, P. Jiménez, I. Caro, J. Tejero, J. Mateo and T. Girbés, *Food Nutr. Sci.*, 2014, **5**, 1765–1775.
5 R. Ranadheera, S. Baines and M. Adams, *Food Res. Int.*, 2010, **43**, 1–7.
6 M. E. Sanders, T. R. Klaenhammer, A. C. Ouwehand, B. Pot, E. Johansen, J. T. Heimbach, M. L. Marco, J. Tennilä, R. P. Ross, C. Franz, N. Pagé, R. D. Pridmore, G. Leyer, S. Salminen, D. Charbonneau, E. Call and I. Lenoir-Wijnkoop, *Ann. N. Y. Acad. Sci.*, 2014, **1309**, 1–18.
7 F. Gomand, F. Borges, J. Burgain, J. Guerin, A.-M. Revol-Junelles and C. Gaiani, *Annu. Rev. Food Sci. Technol.*, 2019, **10**, 285–310.
8 M. E. Sanders and M. L. Marco, *Annu. Rev. Food Sci. Technol.*, 2010, **1**, 65–85.
9 A. C. Ouwehand, E. M. Tuomola, S. Tölkkö and S. Salminen, *Int. J. Food Microbiol.*, 2001, **64**, 119–126.
10 S. B. Doherty, L. Wang, R. P. Ross, C. Stanton, G. F. Fitzgerald and A. Brodkorb, *J. Microbiol. Methods*, 2010, **82**, 301–310.
11 J. P. Arnaud, C. Lacroix, C. Foussereau and L. Choplin, *J. Biotechnol.*, 1993, **29**, 157–175.
12 A. Berzins, M. Toma, M. Rikmanis and U. Viesturs, *Acta Biotechnol.*, 2001, **21**, 155–170.
13 N. Edwards, S. Beeton, A. T. Bull and J. C. Merchuk, *Appl. Microbiol. Biotechnol.*, 1989, **30**, 190–195.
14 A. Ghandi, I. B. Powell, T. Howes, X. D. Chen and B. Adhikari, *J. Food Eng.*, 2012, **113**, 194–200.
15 J. Guerin, J. Burgain, F. Gomand, J. Scher and C. Gaiani, *Crit. Rev. Food Sci. Nutr.*, 2017, **0**, 1–13.
16 J. B. Joshi, C. B. Elias and M. S. Patole, *Chem. Eng. J. Biochem. Eng. J.*, 1996, **62**, 121–141.
17 H. Lange, P. Taillandier and J.-P. Riba, *J. Chem. Technol. Biotechnol.*, 2001, **76**, 501–505.
18 S. Taskila, *Starter Cultures in Food Production*, John Wiley & Sons, Ltd, 2017, pp. 79–100.
19 K. Aziz, M. Tariq and A. Zaidi, *FEMS Microbiol. Lett.*, 2019, **366**, fnz064.

20 S. Yang, H. V. Phan, H. Bustamante, W. Guo, H. H. Ngo and L. D. Nghiem, *Bioresour. Technol.*, 2017, **234**, 439–447.
21 M. Kankainen, L. Paulin, S. Tynkkynen, I. v. Ossowski, J. Reunanen, P. Partanen, R. Satokari, S. Vesterlund, A. P. A. Hendrickx, S. Lebeer, S. C. J. D. Keersmaecker, J. Vanderleyden, T. Hämäläinen, S. Laukkanen, N. Salovuori, J. Ritari, E. Alatalo, R. Korpela, T. Mattila-Sandholm, A. Lassig, K. Hatakka, K. T. Kinnunen, H. Karjalainen, M. Saxelin, K. Laakso, A. Surakka, A. Palva, T. Salusjärvi, P. Auvinen and W. M. d. Vos, *Proc. Natl. Acad. Sci. U. S. A.*, 2009, **106**, 17193–17198.
22 K. A. Kline, S. Fälker, S. Dahlberg, S. Normark and B. Henriques-Normark, *Cell Host Microbe*, 2009, **5**, 580–592.
23 K. A. Kline, K. W. Dodson, M. G. Caparon and S. J. Hultgren, *Trends Microbiol.*, 2010, **18**, 224–232.
24 J. Guerin, J. Bacharouche, J. Burgain, S. Lebeer, G. Francius, F. Borges, J. Scher and C. Gaiani, *Food Hydrocolloids*, 2016, **58**, 35–41.
25 S. Lebeer, I. Claes, H. L. P. Tytgat, T. L. A. Verhoeven, E. Marien, I. v. Ossowski, J. Reunanen, A. Palva, W. M. d. Vos, S. C. J. D. Keersmaecker and J. Vanderleyden, *Appl. Environ. Microbiol.*, 2012, **78**, 185–193.
26 J. Reunanen, I. v. Ossowski, A. P. A. Hendrickx, A. Palva and W. M. d. Vos, *Appl. Environ. Microbiol.*, 2012, **78**, 2337–2344.
27 P. Tripathi, A. Beaussart, D. Alsteens, V. Dupres, I. Claes, I. von Ossowski, W. M. de Vos, A. Palva, S. Lebeer, J. Vanderleyden and Y. F. Dufrêne, *ACS Nano*, 2013, **7**, 3685–3697.
28 P. Tripathi, V. Dupres, A. Beaussart, S. Lebeer, I. J. J. Claes, J. Vanderleyden and Y. F. Dufrêne, *Langmuir*, 2012, **28**, 2211–2216.
29 S. Kiekens, D. Vandenheuvel, G. Broeckx, I. Claes, C. Allonsius, I. De Boeck, S. Thys, J.-P. Timmermans, F. Kiekens and S. Lebeer, *Microb. Biotechnol.*, 2019, 1–7.
30 A. Persat, C. D. Nadell, M. K. Kim, F. Ingremeau, A. Siryaporn, K. Drescher, N. S. Wingreen, B. L. Bassler, Z. Gitai and H. A. Stone, *Cell*, 2015, **161**, 988–997.
31 O. Björnham and O. Axner, *J. Chem. Phys.*, 2009, **130**, 235102.
32 W. M. Weaver, S. Dharmaraja, V. Milisavljevic and D. D. Carlo, *Lab Chip*, 2011, **11**, 883–889.
33 K. I. Pappelbaum, C. Gorzelanny, S. Grässle, J. Suckau, M. W. Laschke, M. Bischoff, C. Bauer, M. Schorpp-Kistner, C. Weidenmaier, R. Schneppenheim, T. Obser, B. Sinha and S. W. Schneider, *Circulation*, 2013, **128**, 50–59.
34 S. Lecuyer, R. Rusconi, Y. Shen, A. Forsyth, H. Vlamakis, R. Kolter and H. A. Stone, *Biophys. J.*, 2011, **100**, 341–350.
35 J. W. Foster, R. M. Cowan and T. A. Maag, *J. Bacteriol.*, 1962, **83**, 330–334.
36 J. S. G. Brookman, *Biotechnol. Bioeng.*, 1975, **17**, 465–479.
37 C. R. Engler and C. W. Robinson, *Biotechnol. Lett.*, 1981, **3**, 83–88.
38 C. R. Engler and C. W. Robinson, *Biotechnol. Bioeng.*, 1981, **23**, 765–780.
39 M. K. Toma, M. P. Ruklisha, J. J. Vanags, M. O. Zeltina, M. P. Lelte, N. I. Galinine, U. E. Viesturs and R. P. Tengerdy, *Biotechnol. Bioeng.*, 1991, **38**, 552–556.
40 M. A. Golowczyc, J. Silva, P. Teixeira, G. L. De Antoni and A. G. Abraham, *Int. J. Food Microbiol.*, 2011, **144**, 556–560.
41 K. D. Young, *Microbiol. Mol. Biol. Rev.*, 2006, **70**, 660–703.
42 K. D. Young, *Curr. Opin. Microbiol.*, 2007, **10**, 596–600.
43 S. Shikano, L. S. Luckinbill and Y. Kurihara, *Microb. Ecol.*, 1990, **20**, 75–84.
44 H. Güde, *Microb. Ecol.*, 1979, **5**, 225–237.
45 K. Jürgens and C. Matz, *Antonie van Leeuwenhoek*, 2002, **81**, 413–434.
46 M. W. Hahn and M. G. Höfle, *Appl. Environ. Microbiol.*, 1999, **65**, 4863–4872.
47 T. Posch, K. Simek, J. Vrba, J. Pernthaler, J. Nedoma, B. Sattler, B. Sonntag and R. Psenner, *Aquat. Microb. Ecol.*, 1999, **18**, 235–246.
48 C. Mercier, E. Domakova, J. Tremblay and S. Kulakauskas, *FEMS Microbiol. Lett.*, 2000, **187**, 47–52.
49 J. Möller, P. Emge, I. A. Vizcarra, P. Kollmannsberger and V. Vogel, *New J. Phys.*, 2013, **15**, 125016.
50 E. Altermann, L. B. Buck, R. Cano and T. R. Klaenhammer, *Gene*, 2004, **342**, 189–197.
51 F. Gomand, F. Borges, D. Salim, J. Burgain, J. Guerin and C. Gaiani, *Food Hydrocolloids*, 2018, **84**, 537–544.
52 S. Lebeer, T. L. A. Verhoeven, G. Francius, G. Schoofs, I. Lambrichts, Y. Dufrêne, J. Vanderleyden and S. C. J. D. Keersmaecker, *Appl. Environ. Microbiol.*, 2009, **75**, 3554–3563.
53 J. Guerin, J. Burgain, G. Francius, S. El-Kirat-Chatel, A. Beaussart, J. Scher and C. Gaiani, *Food Hydrocolloids*, 2018, **82**, 296–303.
54 P. D. Hede, P. Bach and A. D. Jensen, *Chem. Eng. Sci.*, 2008, **63**, 3821–3842.
55 W. Vollmer, D. Blanot and M. A. D. Pedro, *FEMS Microbiol. Rev.*, 2008, **32**, 149–167.
56 C. Pozrikidis, *Boundary Integral and Singularity Methods for Linearized Viscous Flow*, Cambridge University Press, Cambridge, UK, 1992.
57 W. H. Mitchell and S. E. Spagnolie, *J. Comput. Phys.*, 2017, **333**, 462–482.
58 H. Power and G. Miranda, *SIAM J. Appl. Math.*, 1987, **47**, 689–698.
59 M. T. Cabeen and C. Jacobs-Wagner, *Nat. Rev. Microbiol.*, 2005, **3**, 601–610.
60 M. T. Cabeen, G. Charbon, W. Vollmer, P. Born, N. Ausmees, D. B. Weibel and C. Jacobs-Wagner, *EMBO J.*, 2009, **28**, 1208–1219.
61 F. Cava, E. Kuru, Y. V. Brun and M. A. de Pedro, *Curr. Opin. Microbiol.*, 2013, **16**, 731–737.
62 P. F. Clark and W. H. Ruehl, *J. Bacteriol.*, 1919, **4**, 615–629.
63 J. Coley, E. Tarelli, A. R. Archibald and J. Baddiley, *FEBS Lett.*, 1978, **88**, 1–9.
64 A. J. F. Egan and W. Vollmer, *Ann. N. Y. Acad. Sci.*, 2013, **1277**, 8–28.
65 N. B. Grover, C. L. Woldringh, A. Zaritsky and R. F. Rosenberger, *J. Theor. Biol.*, 1977, **67**, 181–193.

66 E. J. Harry, *Mol. Microbiol.*, 2001, **40**, 795–803.
67 E. Harry, L. Monahan and L. Thompson, *International Review of Cytology*, Academic Press, 2006, vol. 253, pp. 27–94.
68 R. F. Rosenberger, N. B. Grover, A. Zaritsky and C. L. Woldringh, *J. Theor. Biol.*, 1978, 73, 711–721.
69 R. D. Turner, A. F. Hurd, A. Cadby, J. K. Hobbs and S. J. Foster, *Nat. Commun.*, 2013, **4**, 1496.
70 J. C. Way, *BioEssays*, 1996, **18**, 99–101.
71 E. P. Previc, *J. Theor. Biol.*, 1970, 27, 471–497.
72 A. Typas, M. Banzhaf, C. A. Gross and W. Vollmer, *Nat. Rev. Microbiol.*, 2012, **10**, 123–136.
73 F. Wong, L. D. Renner, G. Özbaykal, J. Paulose, D. B. Weibel, S. van Teeffelen and A. Amir, *Nat. Microbiol.*, 2017, 2, 17115.
74 S. Badel, T. Bernardi and P. Michaud, *Biotechnol. Adv.*, 2011, **29**, 54–66.
75 H. L. Goldsmith and J. C. Marlow, *J. Colloid Interface Sci.*, 1979, **71**, 383–407.
76 P. A. Aarts, S. A. van den Broek, G. W. Prins, G. D. Kuiken, J. J. Sixma and R. M. Heethaar, *Arteriosclerosis*, 1988, **8**, 819–824.
77 D. Gidaspow and V. Chandra, *Chem. Eng. Sci.*, 2014, **117**, 107–113.
78 C. Nachtigall, C. Berger, T. Kovanovic, D. Wefers, D. Jaros and H. Rohm, *Food Hydrocolloids*, 2019, **97**, 105181.
79 M.-P. Chapot-Chartier and S. Kulakauskas, *Microb. Cell Fact.*, 2014, **13**, S9.
80 J. Delcour, T. Ferain, M. Deghorain, E. Palumbo and P. Hols, *Antonie van Leeuwenhoek*, 1999, pp. 159–184.
81 M. Girard and C. Schaffer-Lequart, *Int. Dairy J.*, 2007, **17**, 666–673.
82 J. Burgain, J. Scher, S. Lebeer, J. Vanderleyden, C. Cailliez-Grimal, M. Corgneau, G. Francius and C. Gaiani, *Food Hydrocolloids*, 2014, **41**, 60–70.
83 S. Kim and S. Karrila, *Microhydrodynamics: Principles and Selected Applications*, Dover Publications, Inc., Mineola, NY, 1991.
84 G. B. Jeffery, *Proc. R. Soc. London, Ser. A*, 1922, **102**, 161–179.
85 Y. F. Dufrêne and A. Persat, *Nat. Rev. Microbiol.*, 2020, **18**, 227–240.
86 A.-K. Tornberg and M. J. Shelley, *J. Comput. Phys.*, 2004, **196**, 8–40.
87 E. J. Hinch, *J. Fluid Mech.*, 1976, **74**, 317–333.
88 Y. Liu, B. Chakrabarti, D. Saintillan, A. Lindner and O. Du Roure, *Proc. Natl. Acad. Sci. U. S. A.*, 2018, **115**, 9438–9443.
89 O. Du Roure, A. Lindner, E. N. Nazockdast and M. J. Shelley, *Annu. Rev. Fluid Mech.*, 2019, **51**, 539–572.
90 B. Audoly and S. Neukirch, *Phys. Rev. Lett.*, 2005, **95**, 095505.
91 J. A. Aström, *Adv. Phys.*, 2006, **55**, 247–278.
92 J. Banasiak, *Phys. D*, 2006, 222, 63–72.
93 J. Banasiak and S. O. Noutchie, *Phys. D*, 2010, **239**, 1422–1435.
94 H. A. Carmona, F. K. Wittel and F. Kun, *Eur. Phys. J.: Spec. Top.*, 2014, **223**, 2369–2382.
95 E. G. El'darov, F. V. Mamedov, V. M. Gol'dberg and G. E. Zaikov, *Int. J. Polym. Mater. Polym. Biomater.*, 1995, **29**, 1–14.
96 P. Forquin and F. Hild, *Advances in Applied Mechanics*, Elsevier, 2010, vol. 44, pp. 1–72.
97 A. Göpferich, *Biomaterials*, 1996, **17**, 103–114.
98 M. Kostoglou, *Chem. Eng. Sci.*, 2000, **55**, 2507–2513.
99 N. V. Mantzaris, *J. Phys. A: Math. Gen.*, 2005, **38**, 5111–5132.
100 Y. Mao, B. Talamini and L. Anand, *Extreme Mech. Lett.*, 2017, **13**, 17–24.
101 E. W. Montroll and R. Simha, *J. Chem. Phys.*, 1940, **8**, 721–726.
102 J. Paturej, A. Milchev, V. G. Rostiashvili and T. A. Vilgis, *EPL*, 2011, **94**, 48003.
103 T. Sjöstrand, *Int. J. Mod. Phys. A*, 1988, **3**, 751–823.
104 J. J. Stickel, R. J. Phillips and R. L. Powell, *J. Rheol.*, 2006, **50**, 379–413.
105 R. M. Ziff and E. D. McGrady, *Macromolecules*, 1986, **19**, 2513–2519.
106 R. M. Ziff and G. Stell, *J. Chem. Phys.*, 1980, **73**, 3492–3499.
107 B. H. Good, M. J. McDonald, J. E. Barrick, R. E. Lenski and M. M. Desai, *Nature*, 2017, **551**, 45–50.
108 A. Amir, F. Babaeipour, D. B. McIntosh, D. R. Nelson and S. Jun, *Proc. Natl. Acad. Sci. U. S. A.*, 2014, **111**, 5778–5783.
109 B. M. Martins and J. C. Locke, *Curr. Opin. Microbiol.*, 2015, **24**, 104–112.
110 Single-cell microbiology, *Nat. Biotechnol.*, 2016, **34**, 1077.
111 A. Bridier, F. Hammes, A. Canette, T. Bouchez and R. Briandet, *Int. J. Food Microbiol.*, 2015, **213**, 2–16.
112 M. Bang, C.-C. Yong, H.-J. Ko, I.-G. Choi and S. Oh, *J. Microbiol. Biotechnol.*, 2018, **28**, 1604–1613.